Stochastic Deep Material Networks as Efficient Surrogates for Stochastic Homogenisation of Non-linear Heterogeneous Materials

Ling Wu[a,], Ludovic Noels[a]

[a] *University of Liege, Department of Aeronautics and Mechanical Engineering, Computational & Multiscale Mechanics of Materials, Allée de la découverte 9, B-4000 Liège, Belgium*

Abstract

The interaction-based Deep Material Network (IB-DMN) is reformulated to decouple the phase volume fraction from the topological parameters of the IB-DMN. Since the phase volume fraction is no longer influenced by the topological parameters, on the one hand the stochastic IB-DMN can predict the response of arbitrary phase volume fraction, and on the other hand the stochastic IB-DMN can be constructed by introducing uncertainties to the topological parameters of a reference IB-DMN, which is trained using data obtained from full-field linear elastic homogenisation, allowing to capture the variability resulting from the micro-structure organisation such as phase clustering.

The non-linear predictions of the proposed stochastic IB-DMN are compared to those from Direct Numerical Simulation (DNS) on 2D Stochastic Volume Elements (SVEs) of unidirectional fibre-reinforced matrix composites in a finite-strain setting. The results from in-plane uni-axial stress and shear tests show that the proposed stochastic IB-DMN is capable of reproducing random non-linear responses with the same stochastic characteristics as the predictions of the DNS conducted on SVE realisations.

Preprint submitted to Computer Methods in Applied Mechanics and Engineering (C) 2025; Licensed under the Creative Commons (CC-BY-NC-ND); formal publication on: 10.1016/j.cma.2025.117994

Keywords: Deep-Material Network, Stochastic, Composites, Stochastic Volume Elements (SVEs), Homogenisation

1. Introduction

For many industrial applications, it is crucial to estimate the probability of rare events in order to assess the structural integrity, beyond considering only the nominal behaviour. In such cases, stochastic virtual testing becomes essential, as experimental campaigns cannot capture these events at a reasonable cost. Therefore, there is a growing interest in the scientific community in performing stochastic virtual testing of structures, particularly those made of heterogeneous materials, such as composites, in order to assess the structural reliability, evaluate the effects of manufacturing conditions on material properties, and support the development of digital twins. One of the main sources of uncertainty in structures made of heterogeneous or engineered materials arises from the the micro-structure due to both geometrical and material variability, including defects.

In order to upscale the uncertainties, a multi-scale analysis is thus required to perform the scale transition between the material and structural scales. To that end, the uncertainty arising from the material heterogeneity has to be described as the spatial variability of the properties at the micro-structural level, with the generated meso-scale virtual specimens serving as stochastic volume elements (SVEs) in a stochastic multi-scale analysis, see the reviews [1, 2].

Email addresses: l.wu@ulg.ac.be (Ling Wu), l.noels@ulg.ac.be (Ludovic Noels)

In some cases, mainly for reversible responses, the evaluation of the stochastic apparent properties of the SVEs can be decoupled from the macro-scale stochastic finite element analyses. This method has been widely used in the context of random elastic media [3, 4], linear micro-polar continua [5–7] or again thermo-elasticity [3, 8]. In these latter references, the homogenisation was mainly used to define the minimum SVE size allowing statistically representative (and thus unique) homogenised properties to be extracted. Nevertheless, the approach was also used to analyze the variability in the homogenised properties in the context of elasticity [9–15], of thermo-elasticity [16], strain-gradient elasticity [17] or elastic phase-field approach [18]. For the latter case, homogenised fracture properties were evaluated through the homogenisation process. Random fields of the homogenised properties can then be generated to conduct stochastic macro-scale simulations. The definition of these random fields can be achieved by considering a moving-window technique when defining the SVEs in order to extract the spatial correlation matrix [11, 14, 15, 18] or by considering the maximum entropy principle [19–22] in order to represent random matrices when the available information is limited. Models of second-order random fields, taking values in some sets of tensors for each of the eight different elasticity symmetry classes of crystal were also developed [23–25].

Considering a spectral stochastic computational scheme, in which the finite-element resolution of the lower-scale BVP is achieved in both the spatial and stochastic domains after applying a Karhunen–Loève expansion of the random material properties, hence defining the interpolation function in the stochastic domain, allows linking the global properties of multi-phase heterogeneous structure to the random material properties of their micro-structural phases [26, 27]. This approach alleviates the need to perform the lower-scale BVP resolution for each micro-structure realisation. Similarly, micro-structure variability, such as the inclusion radius of composite, was accounted for by developing the stochastic-local finite element method [28], which considers usual Lagrangian shape functions in the physical domain and sequences of trigonometric functions in the stochastic domain, or by developing the stochastic-global finite element method [29] in which trigonometric shape functions are considered for both the physical and the stochastic domains. Nevertheless these approaches remain limited in the size of the stochastic domain and mainly to reversible responses.

For general homogenisation-based non-linear multi-scale simulations, in which homogenised properties cannot be clearly identified because of the complex irreversible response of the SVEs, the two scales ought to be solved concurrently, *e.g.* using computational homogenisation to solve the lower-scale boundary value problem (BVP) in a FE^2 context [30, 31], which results in prohibitive computational costs[1]. Therefore, developing *ad hoc* stochastic surrogate or reduced order models to replace the direct numerical solution of the lower-scale BVP defined on the SVEs is desirable, particularly in the context of highly non-linear and irreversible behaviors.

In general, surrogate models are mathematical or micro-mechanical formulations constructed from offline simulations conducted on different SVE realisations. Using Karhunen-Loève series or Polynomial chaos expansions, kriging methods or Gaussian Regression, *etc.*, surrogate models, including in the non-linear range, have been extensively developed in the literature, see the extensive review in [2]. However, these methods cannot generally handle history-dependent non-linearities in a straightforward way, which are common in SVE responses due to plasticity and/or damage. Recently data-driven approaches have emerged as an opportunity to develop such models.

Based on information obtained from offline computations performed on meso-scale BVPs, reduced versions of the models can be created by projecting the governing equations onto suitably selected sub-spaces, such as in the proper orthogonal decomposition (POD) of the displacement field [32]. However, in addition to the challenge of achieving high accuracy with a limited number of modes in the non-linear range, the modes obtained from these offline simulations are specific to a given micro-structure, making it difficult to extend to stochastic behavior. Reduced versions of models can also be based on micro-mechanics approaches with much less variables, such as self-clustering analysis (SCA) [33], where some stochastic effects, like variations in fibre volume fraction and waviness in UD laminate compression, have been studied [34]. However, the interaction matrices are defined for a specific micro-structure, and using different

[1] In the context of elasto-plastic random media [3], or finite elasticity [3], such homogenisation was conducted for random media in order to define the minimum SVE size allowing to extract statistically representative homogenised properties, but it was not used to conduct stochastic multi-scale simulations.

ones requires performing new clustering analyses. Alternatively, an efficient micro-mechanical model, such as the Mean-Field Homogenisation (MFH), can be employed as a stochastic surrogate by associating its parameters to given micro-structure realisations, which however requires a complex identification process [35, 36]. A synthetic micro-structure responses database can be generated by conducting offline simulations of several micro-structure realisations. The synthetic database can then be used to train machine learning algorithms, such as neural networks (NNWs), even in the context of history-dependent problems [37–39]. Theoretically, this approach can also incorporate micro-structure properties as input, in addition to the strain path. However, due to the limited extrapolation capabilities of NNWs, this method requires constructing a large synthetic data-set. Alternatively, when the variability is associated to a clearly identified and quantified micro-structural feature, an interpolation between data-sets obtained for different values of the micro-structure feature can be applied, as suggested in [40] in the context of non-linear electrical conduction. The aforementioned methodologies still have some limitations, including the complexity of generating synthetic databases to train the surrogate models, loss of thermodynamic consistency, and limitations in interpolation or extrapolation capabilities regarding micro-structure features. Specifically, the surrogate is built on data with specific material systems, making it challenging to extend an existing surrogate model to a new material system.

Recently, the Deep Material Network (DMN) method was proposed in [41, 42]. As a homogenisation method based on analytical micro-mechanics models, the DMN is constructed from mechanistic building blocks organised in a binary hierarchical topological structure, with optimised fitting parameters, such as weight ratios and rotation coefficients, through a training process. Once trained using linear elastic data, the DMN is able to predict non-linear responses through a forward homogenisation process and a backward dehomogenisation process evaluating the local unknowns which correspond to the fluctuation fields in the mechanistic building blocks. Because of its thermodynamic consistency, which has been theoretically analysed in [43, 44], the DMN has the ability of extrapolation in terms of the loading path. Besides, since the phase material responses are explicitly modeled using the constitutive material models at the so-called material nodes, the DMN can naturally adapt to different micro-scale material behaviours –*i.e.* constitutive models, including in the non-linear range. The DMN was further extended to material failure [45]. In [46, 47], the original laminate micro-mechanics model was further generalised by defining the interactions from the Hill-Mandel condition, yielding the so-called Interaction-Based Deep Material Network (IB-DMN), improving the training stage. An extensive comparison of the DMN approaches has been provided in [48].

In order to account for variability in the micro-structure geometry, in [49], several specific DMNs trained on micro-structures with varying phase volume fractions were used to construct a micro-structure base, enabling interpolation of new DMNs without requiring additional training. A similar approach was conducted in terms of the Orientation Distribution Function in [49, 50]. The interpolation for complex micro-structure variability, *e.g.* resulting from the fibre organisation such as clustering *etc.*, which cannot be summarised by a single scalar or a tensor, is however not possible since the method assumes statistical representativity. A single-layer feed forward neural network was utilised in [51] to model the dependency of the DMN fitting parameters on the phase fractions of the micro-structure, in which the inclusions are regularly embedded in the matrix material. A graph neural network was employed to extract features from micro-structures in [52], which were then used to provide the DMN fitting parameters through a feed forward neural network trained using linear elastic data, with phase volume fraction constraints applied to its output. In the aforementioned literature, DMNs trained with linear elastic data have been shown to accurately predict the non-linear response of Representative Volume Elements (RVEs).

Since SVEs are stochastic representations of micro-structures with inherent randomness, for DMN to act as a surrogate model in stochastic multi-scale simulations, this paper aims at representing the geometrical uncertainties through a variability of the DMN fitting parameters. To that end, the IB-DMN is reformulated so that the phase volume fraction becomes an input variable while the remaining IB-DMN fitting parameters describe solely the organisation of the micro-structure, such as the phase clustering. As a result, on the one hand the resulting IB-DMN can predict the response for an arbitrary phase volume fraction, and on the other hand a stochastic IB-DMN is constructed by introducing uncertainties to the topological parameters of a reference IB-DMN, which is trained using data obtained from full-field linear elastic homogenisation conducted on different SVE realisations.

As a proof of concept, a reference IB-DMN with a binary tree structure is used to surrogate unidirectional fibre-reinforced composites. The uncertain non-linear response of the SVEs is then shown to be reproduced by the proposed stochastic IB-DMN in which perturbations are applied to the topological parameters of the reference IB-DMN to represent the effect of the micro-structure variability. Nevertheless, this approach has to be seen as a first step toward the use of IB-DMN as stochastic surrogates in multi-scale simulations in which the parameters of the stochastic IB-DMN will be directly correlated to the micro-structure realisation instead of mimicking the effect of the micro-structure variability, but this is out of the scope of this paper.

Organisation of the paper is as follows. We first present in Section 2 the definition of the interaction mechanisms in the context of a homogenisation process. In Section 3, the IB-DMN is presented first in an infinitesimal strain setting for linear training purpose, before being generalised to a finite-strain setting for online simulations. The stochastic IB-DMN is then developed in Section 4. In Section 5, the predictions of the stochastic IB-DMN for the non-linear response of unidirectional (UD) fibre-reinforced matrix composites are then compared to the statistical content obtained by conducting direct numerical simulations on SVE realisations, in which the effects of both the fibre volume fraction and fibres distribution are accounted for. The computational efficiency of the IB-DMN is eventually discussed in Section 6 before drawing some conclusions.

2. Definition of interactions in the context of homogenisation

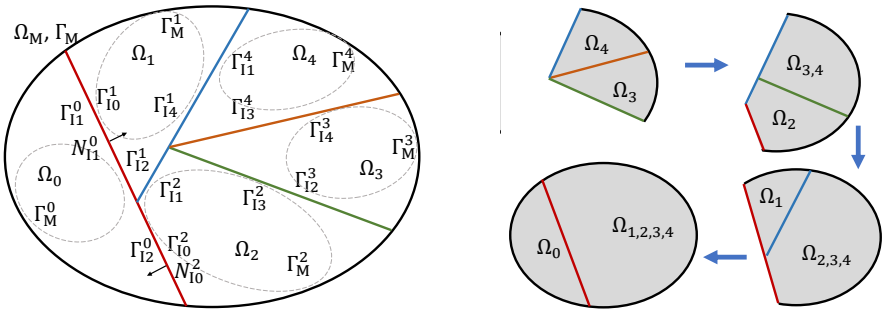

Figure 1: Interaction-Based Deep Material Network: (a) Interactions in domain Ω_{M} which includes $N_{\mathrm{p}}(=5)$ subdomains; and (b) the N_{p}-phase interaction is simplified into sequential two-phase interactions.

2.1. Micro-scale interaction mechanism and homogenisation

In this section, the theoretical background of the interaction mechanism is revisited from the perspective of homogenisation. Considering an aggregation of N_{p} phases within the domain Ω_{M}. Each phase occupies a subdomain Ω_i, such that $\Omega_{\mathrm{M}} = \bigcup_{i=0}^{N_{\mathrm{p}}-1} \Omega_i$, see Fig. 1(a). The outer boundary of Ω_{M} is denoted as $\Gamma_{\mathrm{M}} = \bigcup_{i=0}^{N_{\mathrm{p}}-1} \Gamma_{\mathrm{M}}^i$, where Γ_{M}^i is the outer boundary of phase i with the corresponding outward unit normal vector $\boldsymbol{N}_{\mathrm{M}}^i$. The interfaces between phases, located along the N_{I} planes, are defined as inner boundaries $\Gamma_{\mathrm{I}j}^i$ with their outward unit normal $\boldsymbol{N}_{\mathrm{I}j}^i$, where $j = 0, ..., N_{\mathrm{I}} - 1$ indicates the interface plane, and i denotes the phase connected to it. It should be noted that an interface can be approximated by multiple planes.

The volumes of the domain Ω_{M} and subdomains Ω_i are denoted as V_{M} and V_i, respectively, with $V_{\mathrm{M}} = \sum_{i=0}^{N_{\mathrm{p}}-1} V_i$. Consequently, the volume fraction of phases are defined as $v_i = \frac{V_i}{V_{\mathrm{M}}}$, satisfying $\sum_{i=0}^{N_{\mathrm{p}}-1} v_i = 1.0$. The volume-averaged strain $\boldsymbol{\varepsilon}_{\mathrm{M}}$ and stress $\boldsymbol{\sigma}_{\mathrm{M}}$ for the entire aggregation are related to the volume-averaged strain $\boldsymbol{\varepsilon}_i$ and stress $\boldsymbol{\sigma}_i$ in each phase Ω_i as follows:

$$\boldsymbol{\varepsilon}_{\mathrm{M}} = \sum_{i=0}^{N_{\mathrm{p}}-1} v_i \boldsymbol{\varepsilon}_i \,, \quad \text{and} \quad \boldsymbol{\sigma}_{\mathrm{M}} = \sum_{i=0}^{N_{\mathrm{p}}-1} v_i \boldsymbol{\sigma}_i \,. \tag{1}$$

2.2. Microscopic strain

Using the theory of homogenisation, the displacement field $\boldsymbol{u}_{\mathrm{m}}(\boldsymbol{X}_{\mathrm{m}})$ in Ω_{M}, subject to a homogenised strain $\boldsymbol{\varepsilon}_{\mathrm{M}}$, reads,

$$\boldsymbol{u}_{\mathrm{m}}(\boldsymbol{X}_{\mathrm{m}}) = \boldsymbol{\varepsilon}_{\mathrm{M}} \cdot (\boldsymbol{X}_{\mathrm{m}} - \boldsymbol{X}_{\mathrm{m}_0}) + \boldsymbol{a}(\boldsymbol{X}_{\mathrm{m}}), \quad \boldsymbol{X}_{\mathrm{m}} \in \Omega_{\mathrm{M}}, \tag{2}$$

where $\boldsymbol{X}_{\mathrm{m}_0}$ is a reference point, and $\boldsymbol{a}(\boldsymbol{X}_{\mathrm{m}})$ is the fluctuation field resulting from the heterogeneity of Ω_{M}. The corresponding strain field is given by

$$\boldsymbol{\varepsilon}_{\mathrm{m}}(\boldsymbol{X}_{\mathrm{m}}) = \boldsymbol{\nabla} \otimes^{\mathrm{s}} \boldsymbol{u}_{\mathrm{m}}(\boldsymbol{X}_{\mathrm{m}}) = \boldsymbol{\varepsilon}_{\mathrm{M}} + \boldsymbol{\nabla} \otimes^{\mathrm{s}} \boldsymbol{a}(\boldsymbol{X}_{\mathrm{m}}), \quad \boldsymbol{X}_{\mathrm{m}} \in \Omega_{\mathrm{M}}, \tag{3}$$

where $\boldsymbol{\nabla}$ and $\otimes^{\mathrm{s}}$ are the gradient and symmetric dyadic operators, respectively. Using the expression of microscopic strain, Eq. (3), and the definition of the homogenised strain yields,

$$\boldsymbol{\varepsilon}_{\mathrm{M}} = \frac{1}{V_{\mathrm{M}}} \int_{\Omega_{\mathrm{M}}} \boldsymbol{\varepsilon}_{\mathrm{m}}(\boldsymbol{X}_{\mathrm{m}}) \mathrm{d}V = \sum_{i=0}^{N_{\mathrm{p}}-1} v_i \boldsymbol{\varepsilon}_{\mathrm{M}} + \frac{1}{V_{\mathrm{M}}} \sum_{i=0}^{N_{\mathrm{p}}-1} \int_{\Omega_i} \boldsymbol{\nabla} \otimes^{\mathrm{s}} \boldsymbol{a}(\boldsymbol{X}_{\mathrm{m}}) \mathrm{d}V \,, \tag{4}$$

and leads to

$$\sum_{i=0}^{N_{\mathrm{p}}-1} \int_{\Omega_i} \boldsymbol{\nabla} \otimes^{\mathrm{s}} \boldsymbol{a}(\boldsymbol{X}_{\mathrm{m}}) \mathrm{d}V = \boldsymbol{0} \,, \tag{5}$$

according to Eq. (1). Applying Gauss' theorem, Eq.(5)[2] can be rewritten as,

$$\sum_{i=0}^{N_{\mathrm{p}}-1} \left[\int_{\Gamma_{\mathrm{M}}^i} \boldsymbol{a}(\boldsymbol{X}_{\mathrm{m}}) \otimes^{\mathrm{s}} \boldsymbol{N}_{\mathrm{M}}^i(\boldsymbol{X}_{\mathrm{m}}) \mathrm{d}s + \sum_{\forall \Gamma_{\mathrm{I}_j}^i \neq \emptyset} \int_{\Gamma_{\mathrm{I}_j}^i} \boldsymbol{a}(\boldsymbol{X}_{\mathrm{m}}) \otimes^{\mathrm{s}} \boldsymbol{N}_{\mathrm{I}_j}^i \mathrm{d}s \right] = \boldsymbol{0} \,. \tag{6}$$

Since for any inner boundaries with $\Gamma_{\mathrm{I}_j}^i \neq \emptyset$ two adjacent subdomains have opposite outward unit normals, the second term in Eq. (6) is always zero for a continuous field $\boldsymbol{a}(\boldsymbol{X}_{\mathrm{m}})$. The zero-value of the first term can be achieved by applying a specially defined boundary condition classical for homogenisation theory, such as a kinematic constraint on the outer boundary of Γ_{M},

$$\boldsymbol{a}(\boldsymbol{X}_{\mathrm{m}}) = \boldsymbol{0} \,, \quad \text{for } \boldsymbol{X}_{\mathrm{m}} \in \Gamma_{\mathrm{M}} \text{ and } \Gamma_{\mathrm{M}} = \bigcup_{i=0}^{N_{\mathrm{p}}-1} \Gamma_{\mathrm{M}}^i \,, \tag{7}$$

or by selecting a periodic fluctuation $\boldsymbol{a}(\boldsymbol{X}_{\mathrm{m}})$ at the outer boundary, in which case the outer boundary can be treated as an inner boundary of an infinite periodic domain, $\Gamma_{\mathrm{M}} = \emptyset$. Then, along with the analysis of Eq. (6), Eq. (4) can be rewritten as

$$\boldsymbol{\varepsilon}_{\mathrm{M}} \quad = \quad \sum_{i=0}^{N_{\mathrm{p}}-1} v_i \left[\boldsymbol{\varepsilon}_{\mathrm{M}} + \frac{1}{V_i} \sum_{\forall \Gamma_{\mathrm{I}_j}^i \neq \emptyset} \int_{\Gamma_{\mathrm{I}_j}^i} \boldsymbol{a}(\boldsymbol{X}_{\mathrm{m}}) \otimes^{\mathrm{s}} \boldsymbol{N}_{\mathrm{I}_j}^i \mathrm{d}s \right] . \tag{8}$$

By comparing Eq. (8) with Eq. (1), we obtain the following result for any continuous field $\boldsymbol{a}(\boldsymbol{X}_{\mathrm{m}})$,

$$\boldsymbol{\varepsilon}_i \quad = \quad \boldsymbol{\varepsilon}_{\mathrm{M}} + \frac{1}{V_i} \sum_{\forall \Gamma_{\mathrm{I}_j}^i \neq \emptyset} \int_{\Gamma_{\mathrm{I}_j}^i} \boldsymbol{a}(\boldsymbol{X}_{\mathrm{m}}) \otimes^{\mathrm{s}} \boldsymbol{N}_{\mathrm{I}_j}^i \mathrm{d}s \,. \tag{9}$$

[2]We consider Ω_i, $\Gamma_{\mathrm{I}_j}^i$, $\boldsymbol{N}_{\mathrm{I}_j}^i$ in the reference configuration since we are in an infinitesimal deformation setting.

Defining

$$\boldsymbol{a}_j = \frac{1}{s_j^i} \int_{\Gamma_{\mathrm{I}_j^i}} \boldsymbol{a}(\boldsymbol{X}_{\mathrm{m}}) \mathrm{d}s \,, \tag{10}$$

where the surface parameter is defined as $s_j^i = \int_{\Gamma_{\mathrm{I}_j^i}} \mathrm{d}s$ for $\Gamma_{\mathrm{I}_j^i} \neq \emptyset$, the volume-averaged strain in each phase can be formulated following

$$\boldsymbol{\varepsilon}_i \;\; = \;\; \boldsymbol{\varepsilon}_{\mathrm{M}} + \frac{1}{V_i} \sum_{\forall \Gamma_{\mathrm{I}_j^i} \neq \emptyset} s_j^i \boldsymbol{a}_j \otimes^{\mathrm{s}} \boldsymbol{N}_{\mathrm{I}_j^i} \,. \tag{11}$$

Physically, this equation represents the strain concentration tensor, which expresses the relation between the lower-scale strain distribution, here the volume-averaged strain $\boldsymbol{\varepsilon}_i$ in phase Ω_i, and the macro-scale strain $\boldsymbol{\varepsilon}_{\mathrm{M}}$ through the perturbation field $\boldsymbol{a}(\boldsymbol{X}_{\mathrm{m}})$, Eq. (2), here its surface-averaged value $\boldsymbol{a}_j$, Eq. (10).

2.3. Hill-Mandel condition

The energy consistency between the scales implies that

$$\boldsymbol{\sigma}_{\mathrm{M}} : \delta\boldsymbol{\varepsilon}_{\mathrm{M}} = \sum_{i=0}^{N_{\mathrm{p}}-1} v_i \boldsymbol{\sigma}_i : \delta\boldsymbol{\varepsilon}_i \,. \tag{12}$$

This equation expresses that the stress power at the macro-scale, the left-hand side, is equivalent to the stress power at the lower-scale, the right-hand side, which is formulated through the volume-averaged fields in the phases Ω_i. This relation is the keystone of homogenisation theory which is required to ensure thermodynamic consistency.

Using Eq. (11), this last result is rewritten as

$$\boldsymbol{\sigma}_{\mathrm{M}} : \delta\boldsymbol{\varepsilon}_{\mathrm{M}} = \sum_{i=0}^{N_{\mathrm{p}}-1} v_i \boldsymbol{\sigma}_i : \delta\boldsymbol{\varepsilon}_{\mathrm{M}} + \sum_{i=0}^{N_{\mathrm{p}}-1} \sum_{\forall \Gamma_{\mathrm{I}_j^i} \neq \emptyset} \frac{v_i s_j^i}{V_i} \boldsymbol{\sigma}_i : \left(\delta\boldsymbol{a}_j \otimes^{\mathrm{s}} \boldsymbol{N}_{\mathrm{I}_j^i} \right) \,, \tag{13}$$

or again, using Eq. (1) and the symmetric nature of the Cauchy stress tensor, as

$$\sum_{i=0}^{N_{\mathrm{p}}-1} \sum_{\forall \Gamma_{\mathrm{I}_j^i} \neq \emptyset} \frac{v_i s_j^i}{V_i} \boldsymbol{\sigma}_i : \left(\boldsymbol{N}_{\mathrm{I}_j^i} \otimes^{\mathrm{s}} \delta\boldsymbol{a}_j \right) = 0 \,. \tag{14}$$

Equation (14) constitutes the weak form of the approximation, which is stated as finding the solutions for $\boldsymbol{a}_k$, $k = 0, ..., N_{\mathrm{I}} - 1$, in Eq. (11), which yield the averaged stresses $\boldsymbol{\sigma}_i$, $i = 0, ..., N_{\mathrm{p}} - 1$, that satisfy Eq. (14) for arbitrary $\delta\boldsymbol{a}_j$.

To close the system, we apply a constitutive behaviour in each phase Ω_i to relate the averaged stress to the averaged strain following

$$\boldsymbol{\sigma}_i = \boldsymbol{\sigma}^p \left(\boldsymbol{\varepsilon}_i(\boldsymbol{a}_j);\, \boldsymbol{\psi}_i \right) \;, \text{ for } i = 0, \ldots, N_{\mathrm{p}} - 1 \,, \tag{15}$$

where $\boldsymbol{\psi}_i$ is the set of internal variables in the case of a non-linear behaviour, and where $\boldsymbol{\sigma}^p$ is the constitutive behaviour considered for phase Ω_i.

2.4. Microscopic stress

In the absence of dynamics and body forces, the equilibrium equation for the aggregate, Ω_{M}, is given by

$$\boldsymbol{\nabla} \cdot \boldsymbol{\sigma}_{\mathrm{m}}(\boldsymbol{X}_{\mathrm{m}}) = \boldsymbol{0} \,, \text{ for } \boldsymbol{X}_{\mathrm{m}} \in \Omega_{\mathrm{M}} \,, \tag{16}$$

under the Dirichlet boundary condition, Eq. (7), or periodic boundary condition on Γ_{M}. This equation can be rewritten

$$\mathbf{0} = \frac{1}{V_{\mathrm{M}}} \int_{\Omega_{\mathrm{M}}} \boldsymbol{\nabla} \cdot \boldsymbol{\sigma}_{\mathrm{m}}(\boldsymbol{X}_{\mathrm{m}}) \mathrm{d}V \,. \tag{17}$$

Applying Gauss's theorem, Eq. (17) can be rewritten as

$$\sum_{i=0}^{N_{\mathrm{p}}-1} \left[\int_{\Gamma_{\mathrm{M}}^i} \boldsymbol{\sigma}_{\mathrm{m}}(\boldsymbol{X}_{\mathrm{m}}) \cdot \boldsymbol{N}_{\mathrm{M}}^i(\boldsymbol{X}_{\mathrm{m}}) \mathrm{d}s + \sum_{\forall \Gamma_{\mathrm{I}_j}^i \neq \emptyset} \int_{\Gamma_{\mathrm{I}_j}^i} \boldsymbol{\sigma}_{\mathrm{m}}(\boldsymbol{X}_{\mathrm{m}}) \cdot \boldsymbol{N}_{\mathrm{I}_j}^i \mathrm{d}s \right] = \mathbf{0} \,. \tag{18}$$

The first term vanishes for consistent boundary conditions like periodic boundary conditions. The remaining equilibrium equation is then approximated by considering the averaged stress $\boldsymbol{\sigma}_i$ in each subdomain Ω_i, $i = 0, ..., N_{\mathrm{p}} - 1$, which results on the interface Γ_{I} in

$$\sum_{i=0}^{N_{\mathrm{p}}-1} \int_{\Gamma_{\mathrm{I}_j}^i} \boldsymbol{\sigma}_i \cdot \boldsymbol{N}_{\mathrm{I}_j}^i \mathrm{d}s = \sum_{i=0}^{N_{\mathrm{p}}-1} s_j^i \boldsymbol{\sigma}_i \cdot \boldsymbol{N}_{\mathrm{I}_j}^i = \mathbf{0} \,, \text{ for } j = 0, ..., N_{\mathrm{I}} - 1 \,. \tag{19}$$

This set of equilibrium Eqs. (19) of the interfaces corresponds to the set of equations resulting from the Hill-Mandel Eq. (14) for arbitrary values of $\delta \boldsymbol{a}_j$. This is thus the weak form of the problem: since the homogenised stress $\boldsymbol{\sigma}_{\mathrm{M}}$ of the aggregate can be evaluated by Eq. (1), the key problem becomes finding the solutions for $\boldsymbol{a}_k$, $k = 0, ..., N_{\mathrm{I}} - 1$, in Eq. (11), which yield the averaged stresses $\boldsymbol{\sigma}_i$, $i = 0, ..., N_{\mathrm{p}} - 1$, that satisfy Eq. (19).

3. Interaction-Based Deep Material Network (IB-DMN)

The approximation set in Section 2.4 can provide a highly accurate solution to the aggregate homogenisation problem if the interaction structure is well defined. The accuracy of the approximate solution depends on the predefined interaction structure, such as the division of Ω_{M} in subdomains Ω_i, with $i = 0, ..., N_{\mathrm{p}} - 1$ and in interfaces $\Gamma_{\mathrm{I}_j}^i \neq \emptyset$, with $j = 0, ..., N_{\mathrm{I}} - 1$, as well as the identification of the corresponding topological parameters, such as the subdomain volume fractions v_i, the surface area s_j^i of the subdomain i on an interface j, and the normal $\boldsymbol{N}_{I_j}^i$ to the interface. Once the interactions structure is defined, the topological parameters, denoted by $\mathcal{G} = \{v_i, s_j^i, \boldsymbol{N}_{\mathrm{I}_j}^i \,|i = 0, ..., N_{\mathrm{p}} - 1 \text{ and } j = 0, ..., N_{\mathrm{I}} - 1\}$, can be determined through a data driven training process.

However, dividing into subdomains is not a straightforward process and can be challenging. As illustrated in Fig. 1(b), a direct division in subdomains can be avoided by using a sequential two-phase approach. We start this section by considering a one-level interaction considering only two subdomains. Building on this result, we introduce the multi-level interactions binary tree structure, first in the infinitesimal strain setting with a view of linear training and then in a generalised finite-strain setting for online simulations. In such a binary tree structure made of 2-phase interactions, each interface $\Gamma_{\mathrm{I}_j}^i \neq \emptyset$, considered in Eqs. (18) and (19), is shared by only two domains Ω_i and Ω_j and defined by the normal directions $\boldsymbol{N}_{I_j}^i = -\boldsymbol{N}_{I_i}^j$. Training and online simulations are then illustrated in the case of unidirectional (UD) composite volume elements of different volume fractions.

3.1. One-level two-phase planar interaction and simplified topological parameters

For illustration, let us first consider an aggregate domain Ω_{M} of arbitrary shape, where only two phases occupy the subdomains Ω_{A} and Ω_{B}, such that $\Omega_{\mathrm{M}} = \Omega_{\mathrm{A}} \bigcup \Omega_{\mathrm{B}}$, see Fig. 2(a). The outer boundary Γ_{M} is subdivided as $\Gamma_{\mathrm{M}} = \Gamma_{\mathrm{M}}^{\mathrm{A}} + \Gamma_{\mathrm{M}}^{\mathrm{B}}$. A two-phase system with planar interaction can be viewed as a general formulation of laminate theory. The volume fractions of both phases are respectively v_{A} and v_{B} with $v_{\mathrm{A}} + v_{\mathrm{B}} = 1.0$. The interface between the phases is approximated by a planar surface Γ_{AB}, with the outward

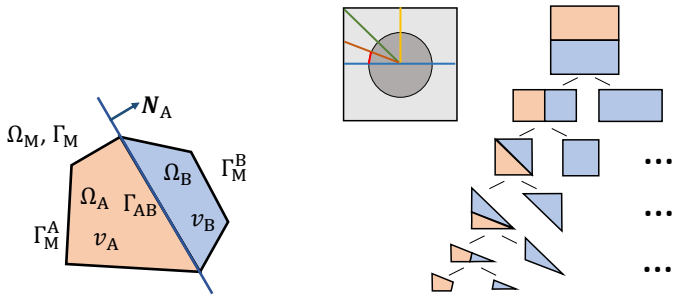

(a) (b)

Figure 2: Binary interaction for a two-phase composite micro-structure: (a) Interactions between 2 subdomains, Ω_A and Ω_B, in the domain Ω_M; and (b) Direct subdivision of a micro-structure (by opposition to the data-driven approach followed in this paper).

unit normal $\boldsymbol{N}_A$ for domain Ω_A and $\boldsymbol{N}_B$ for Ω_B, where $\boldsymbol{N}_B = -\boldsymbol{N}_A$. Recalling the strain expression in each phase from Eq. (11), and using the simplified notation for the two-phase aggregate, yield

$$\boldsymbol{\varepsilon}_A = \boldsymbol{\varepsilon}_M + \frac{1}{v_A}\frac{s_{AB}}{V_M}\boldsymbol{a} \otimes^s \boldsymbol{N}_A\,, \text{ and } \boldsymbol{\varepsilon}_B = \boldsymbol{\varepsilon}_M - \frac{1}{v_B}\frac{s_{AB}}{V_M}\boldsymbol{a} \otimes^s \boldsymbol{N}_A\,, \tag{20}$$

where s_{AB} is the surface area of Γ_{AB}. Since $\frac{s_{AB}}{V_M}$ remains constant for a given two-phase aggregate, we can further define the normalised fluctuation $\hat{\boldsymbol{a}} = \frac{s_{AB}}{V_M}\boldsymbol{a}$, which simplifies the last expressions to

$$\boldsymbol{\varepsilon}_A = \boldsymbol{\varepsilon}_M + \frac{1}{v_A}\hat{\boldsymbol{a}} \otimes^s \boldsymbol{N}_A\,, \text{ and } \boldsymbol{\varepsilon}_B = \boldsymbol{\varepsilon}_M - \frac{1}{1.0 - v_A}\hat{\boldsymbol{a}} \otimes^s \boldsymbol{N}_A\,. \tag{21}$$

The expressions in Eq. (21) show that the volume-averaged strains in each subdomain are influenced solely by the direction $\boldsymbol{N}_A$ of their interface and by the normalised fluctuation $\hat{\boldsymbol{a}}$ along it. The shapes of the subdomains, however, have no effect: only their respective volume fractions v_A and $v_B = 1 - v_A$ have.

For a linear elastic material system, let $\mathbb{C}_A$ and $\mathbb{C}_B$ represent the elasticity tensors of the two interacting phases, and let $\mathbb{C}_M$ represent that of the homogenised material. The equilibrium equation (19) can be simplified on the interface as

$$\boldsymbol{N}_A \cdot \left[\mathbb{C}_A : \left(\boldsymbol{\varepsilon}_M + \frac{1}{v_A}\hat{\boldsymbol{a}} \otimes^s \boldsymbol{N}_A\right) - \mathbb{C}_B : \left(\boldsymbol{\varepsilon}_M - \frac{1}{1.0 - v_A}\hat{\boldsymbol{a}} \otimes^s \boldsymbol{N}_A\right)\right] = \boldsymbol{0}\,. \tag{22}$$

Using Voigt notation $\boldsymbol{\varepsilon} = [\varepsilon_{00}, \varepsilon_{11}, \varepsilon_{22}, 2\varepsilon_{01}, 2\varepsilon_{02}, 2\varepsilon_{12}]^T$ for the strain tensor, and the matrix expression $\mathbf{N}$ of a normal $\boldsymbol{N}$, which reads

$$\mathbf{N} = \begin{bmatrix} N_0 & 0 & 0 & N_1 & N_2 & 0 \\ 0 & N_1 & 0 & N_0 & 0 & N_2 \\ 0 & 0 & N_2 & 0 & N_0 & N_1 \end{bmatrix}^T\,, \tag{23}$$

the tensor operation $\hat{\boldsymbol{a}} \otimes^s \boldsymbol{N}_A$ can be expressed under the matrix form $\mathbf{N}_A\hat{\mathbf{a}}$, where $\hat{\mathbf{a}} = [\hat{a}_0, \hat{a}_1, \hat{a}_2]^T$. Using Voigt notation for the elasticity tensors $\mathbf{C}$, the matrix form of Eq. (22) reads

$$\mathbf{N}_A^T\left(\frac{1}{v_A}\mathbf{C}_A + \frac{1}{1.0 - v_A}\mathbf{C}_B\right)\mathbf{N}_A\hat{\mathbf{a}} = \mathbf{N}_A^T\left(\mathbf{C}_B - \mathbf{C}_A\right)\boldsymbol{\varepsilon}_M\,. \tag{24}$$

The interface fluctuation $\hat{\mathbf{a}}$ can then be evaluated directly using

$$\begin{aligned} \hat{\mathbf{a}} &= \mathcal{K}^{-1}\mathcal{L}\boldsymbol{\varepsilon}_M\,, \quad \text{with} \\ \mathcal{K} &= \mathbf{N}_A^T\left(\frac{1}{v_A}\mathbf{C}_A + \frac{1}{1.0 - v_A}\mathbf{C}_B\right)\mathbf{N}_A \text{ and } \mathcal{L} = \mathbf{N}_A^T\left(\mathbf{C}_B - \mathbf{C}_A\right)\,. \end{aligned} \tag{25}$$

According to Eq. (1), and using Eq. (25), the homogenised stress, expressed in Voigt notation, is given by

$$\begin{aligned}\boldsymbol{\sigma}_{\mathrm{M}} &= v_{\mathrm{A}}\mathbf{C}_{\mathrm{A}}\left(\boldsymbol{\varepsilon}_{\mathrm{M}}+\frac{1}{v_{\mathrm{A}}}\mathbf{N}_{\mathrm{A}}\hat{\mathbf{a}}\right)+(1.0-v_{\mathrm{A}})\mathbf{C}_{\mathrm{B}}\left(\boldsymbol{\varepsilon}_{\mathrm{M}}-\frac{1}{1.0-v_{\mathrm{A}}}\mathbf{N}_{\mathrm{A}}\hat{\mathbf{a}}\right)\\ &= \left[v_{\mathrm{A}}\mathbf{C}_{\mathrm{A}}+(1.0-v_{\mathrm{A}})\mathbf{C}_{\mathrm{B}}+(\mathbf{C}_{\mathrm{A}}-\mathbf{C}_{\mathrm{B}})\,\mathbf{N}_{\mathrm{A}}\mathcal{K}^{-1}\mathcal{L}\right]\boldsymbol{\varepsilon}_{\mathrm{M}}\,. \end{aligned} \tag{26}$$

Then, the homogenised elasticity tensor $\mathbf{C}_{\mathrm{M}}$ can be extracted from Eq. (26) and reads, in Voigt notation,

$$\mathbf{C}_{\mathrm{M}} = v_{\mathrm{A}}\mathbf{C}_{\mathrm{A}}+(1.0-v_{\mathrm{A}})\,\mathbf{C}_{\mathrm{B}}+(\mathbf{C}_{\mathrm{A}}-\mathbf{C}_{\mathrm{B}})\,\mathbf{N}_{\mathrm{A}}\mathcal{K}^{-1}\mathcal{L}\,. \tag{27}$$

From Eq. (27), it can be seen that the topological parameters for a two-phase aggregate reduce to $\mathcal{G}^2 = \{v_{\mathrm{A}},\, \boldsymbol{N}_{\mathrm{A}}\}$.

3.2. Multi-level two-phase interactions

For more complex multi-level interaction structures, the sequential interaction mechanism can be represented by a tree structure, or so-called Deep Material network (DMN), and applied to a heterogeneous material with multiple phases. For complex multiple-phase material systems, such as woven composites [53], a carefully predefined tree structure is required. In contrast, for a simple two-phase heterogeneous material, using a binary tree structure is a straightforward choice.

To provide an intuitive illustration of a binary tree structure, a simple unidirectional fibre-reinforced matrix composite volume element is used in Fig. 2(b). Only one branch of the tree is shown in details, where the two fundamental phases –matrix and fibre– are located at the bottom of the tree. The final composite node is obtained through a sequential interaction mechanism. It can be seen that a part of the matrix/fibre interface is approximated by a straight line in 2D, and the strains at the two bottom or material nodes are uniform and correspond to volume-averaged values on the volumes represented by those nodes. However, in the IB-DMN approach, instead of using such a direct subdivision of the micro-structure –such a strategy was actually followed in [54]– as illustrated in Fig. 2(b), an abstract binary tree is employed as illustrated in Fig. 3(a). This abstract tree subdivision, and the definition of the topological parameters defined by the normals and volume fractions, arises from a data-driven approach, *i.e.* through a training process using off-line direct numerical simulation results performed on the micro-structure. In this tree, basic material nodes experiencing similar strains are merged, with modified interface orientations, to achieve a more compact IB-DMN.

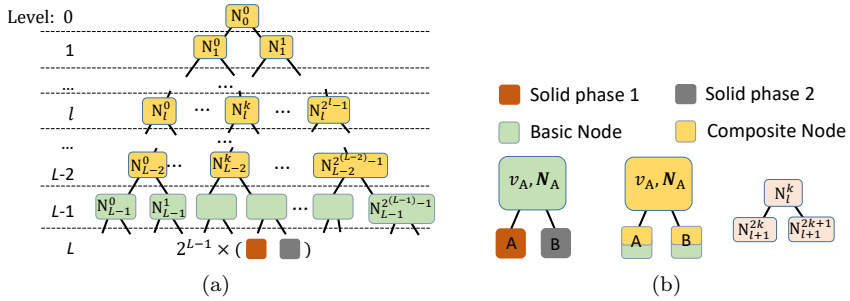

Figure 3: Definition of the Interaction-Based Deep Material Network: (a) Binary tree structure of microscopic interaction mechanism; and (b) Numbering of nodes and their corresponding topological parameters.

In a tree structure with L levels, the nodes are identified by their locations in the tree, denoted as N_l^k, where $l = 0,\, 1,\, ...,\, L$ represents the level and $k = 0,\, 1,\, ...,\, \left(2^l - 1\right)$ represents the position within that level, see Fig. 3(a).

The $N_p = 2^L$ nodes at the bottom level of the tree, *i.e.* nodes of index N_L^k, are called material nodes and correspond to a homogeneous phase whose behaviour follows a known constitutive law (15), as illustrated in Fig. 3. In the case of a two-phase heterogeneous material, there are two such constitutive models $\boldsymbol{\sigma}^0\left(\boldsymbol{\varepsilon}_i;\, \boldsymbol{\psi}_i\right)$

Table 1: Two-phase interaction function

FUN $\left(l,\, \mathbf{C}_0\,, \mathbf{C}_\mathrm{I}\,, \mathcal{G}^2\left(\mathrm{N}_l^k\right)\right)$:
  If: $l < L-1$:
    $\mathbf{C}_\mathrm{A} = \mathrm{FUN}\left(l+1,\, \mathbf{C}_0\,, \mathbf{C}_\mathrm{I}\,, \mathcal{G}^2\left(\mathrm{N}_{l+1}^{2k}\right)\right)$;
    $\mathbf{C}_\mathrm{B} = \mathrm{FUN}\left(l+1,\, \mathbf{C}_0\,, \mathbf{C}_\mathrm{I}\,, \mathcal{G}^2\left(\mathrm{N}_{l+1}^{2k+1}\right)\right)$;
  Else:
    For a two-phase material $\mathbf{C}_\mathrm{A} = \mathbf{C}_0$, and $\mathbf{C}_\mathrm{B} = \mathbf{C}_\mathrm{I}$
  Compute $\mathbf{C}_\mathrm{M}$ using Eqs. (25) and (27).
  Return $\mathbf{C}_\mathrm{M}$

for $i = 0, 2, ..., 2^L - 2$ and $\boldsymbol{\sigma}^\mathrm{I}\left(\boldsymbol{\varepsilon}_i;\, \boldsymbol{\psi}_i\right)$ for $i = 1, 3, ..., 2^L - 1$. In particular, the elasticity tensors of the phases are denoted by $\mathbf{C}_0$ and $\mathbf{C}_\mathrm{I}$, and the volume fraction of the second material phase in the heterogeneous material –*i.e.* for all the material nodes of the structure– by v_I;

The other nodes, *i.e.* nodes of index N_l^k where $l = 0, 1, ..., L-1$, are described by their topological parameters, as detailed in Section 3.1 and with their numbering illustrated in Fig. 3(b). We use $\mathcal{G}^2\left(\mathrm{N}_l^k\right)$ to represent the topological parameters, $\{v_\mathrm{A},\, \boldsymbol{N}_\mathrm{A}\}$, associated to the node N_l^k.

3.2.1. Homogenised elasticity tensor

The homogenised elasticity tensor of the two-phase heterogeneous material can be evaluated using the interaction mechanism defined by the tree structure and the topological parameters associated to its nodes, $\mathcal{G}^2\left(\mathrm{N}_l^k\right)$, where $l = 0, 1, ..., L-1$ and $k = 0, 1, ..., \left(2^l - 1\right)$.

Following the derivation in Section 3.1, we define a general two-phase interaction function, see Table 1. Using $\mathbf{C}_0$, $\mathbf{C}_\mathrm{I}$, $\mathcal{G}^2\left(\mathrm{N}_l^k\right)$, where $l = 0, 1, ..., L-1$ and $k = 0, 1, ..., \left(2^l - 1\right)$, as input, the homogenised elasticity tensor is expressed as,

$$\mathbf{C}_\mathrm{M} = \mathrm{FUN}\left(l = 0,\, \mathbf{C}_0,\, \mathbf{C}_\mathrm{I},\, \mathcal{G}^2\left(\mathrm{N}_0^0\right)\right)\,, \tag{28}$$

where $\mathbf{C}_\mathrm{M}$ is evaluated through recursive calls to the function "FUN()".

3.2.2. Linear elastic training of the IB-DMN

To obtain an accurate DMN representation of a heterogeneous material, the topological parameters $\mathcal{G}^2\left(\mathrm{N}_l^k\right)$ of the IB-DMN need to be determined properly. A training process aiming at minimising a loss function can be applied to that end. The loss function can be defined as

$$Loss(\hat{\mathbf{C}}_\mathrm{M}\,, \mathbf{C}_\mathrm{M}) = \frac{1}{n}\sum_{s=0}^{n-1} \frac{\|\hat{\mathbf{C}}_\mathrm{M}(\mathbf{C}_0^s\,, \mathbf{C}_\mathrm{I}^s) - \mathbf{C}_\mathrm{M}(\mathbf{C}_0^s\,, \mathbf{C}_\mathrm{I}^s;\, \mathcal{G}^2)\|}{\|\hat{\mathbf{C}}_\mathrm{M}(\mathbf{C}_0^s\,, \mathbf{C}_\mathrm{I}^s)\|} + \frac{\lambda}{2}(\tilde{v}_\mathrm{I} - v_\mathrm{I})^2\,, \tag{29}$$

where $\|\bullet\|$ refers to the Frobenius norm, $\hat{\mathbf{C}}_\mathrm{M}$ are the training data obtained using Direct Numerical Simulations (DNSs) for different realisations of the phases elastic properties $\mathbf{C}_0^s$ and $\mathbf{C}_\mathrm{I}^s$, n is the number of data used in the training process and $\mathbf{C}_\mathrm{M}\left(\mathbf{C}_0^s\,, \mathbf{C}_\mathrm{I}^s;\, \mathcal{G}^2\right)$, $s = 0, ..., n-1$, are the predictions of the IB-DMN obtained from Eq. (28) for the different realisations of $\mathbf{C}_0^s$ and $\mathbf{C}_\mathrm{I}^s$. We also use the notation $\mathcal{G}^2$ as the aggregate of $\mathcal{G}^2\left(\mathrm{N}_l^k\right)$ with $l = 0, 1, ..., L-1$ and $k = 0, 1, ..., \left(2^l - 1\right)$. The last term in Eq. (29) is a penalty with the parameter λ, which imposes a constraint on the topological parameters to ensure that the final volume fraction $\tilde{v}_\mathrm{I}$ of the material phase "I" in the IB-DMN remains consistent with the volume fraction v_I of that material phase in the reference heterogeneous material.

PyTorch is used to implement the "FUN()" reported in Table 1 and to minimise the loss function (29). The "AdamW" algorithm is selected to conduct the optimisation process.

3.3. Extension of DMN to non-linear problems in a finite-strain setting

In Section 3.1, the phase interactions were formulated under an infinitesimal strain setting, from which closed-form expressions of the homogenised properties could be obtained, leading to a fast training process of the IB-DMN. In a (IB-)DMN approach, the tree structure illustrated in Fig. 3 exemplifies the role of the different nodes. Nodes at the level L, the so-called material nodes, are responsible for the integration of the phase constitutive behaviours. Nodes at level $l < L$ are characterised by their topological parameters $\mathcal{G}^2\left(\mathrm{N}_l^k\right)$, which are fitting parameters. In order to evaluate these topological fitting parameters, a training has been performed by considering different material responses, although in the linear range, of the micro-structure phases as detailed in Section 3.2.2. As a result, the topological parameters $\mathcal{G}^2\left(\mathrm{N}_l^k\right)$ are representative of the micro-structure organisation solely, and do not depend on the material response of the phases. In consequence, since the IB-DMN illustrated in Fig. 3 with the topological parameters $\mathcal{G}^2\left(\mathrm{N}_l^k\right)$ obtained from a linear training, on the one hand represents the micro-structure organisation independently of the phases material response, and on the other hand is thermodynamically consistent –the Hill-Mandel condition is satisfied and the material nodes integrate a consistent material model, the trained IB-DMN can readily be used in the online stage to simulate non-linear and irreversible material responses of the same micro-structure organisation by considering such material models at the material nodes level.

We however note that, in some cases, more accurate predictions could be reached with a non-linear training process [47], but this requires a non-linear equation (the equilibrium equation at the interface) to be solved at each training epoch, which significantly slows down the training process and prevents the IB-DMN from being trained using batch data (which will be required to build the stochastic IB-DMN in Section 4).

Besides, we consider in the non-linear regime a finite-strain setting. The extension of the interaction-based DMN to a finite-strain setting is built on the fact that the micro-structure remains constant in the reference configuration, meaning that the elasticity tensor at zero-deformation in a finite-strain setting corresponds to the one of an infinitesimal setting. The topological parameters $\mathcal{G}^2\left(\mathrm{N}_l^k\right)$ obtained from a linear training thus represent the interaction mechanisms in the micro-structure of a heterogeneous material, allowing their use for non-linear simulations in a finite-strain setting. This allows for a direct application of the existing network structure to non-linear problems, with the primary modifications being made to the strain measures and constitutive models used within the network. Using the deformation gradient $\mathbf{F}$, which is defined as the gradient of the deformation mapping $\boldsymbol{x}$ with respect to each component of the reference material point $\boldsymbol{X}$ $\left(F_{iJ} = \frac{\partial x_i}{\partial X_J}\right)$, and the first Piola-Kirchhoff stress tensor $\mathbf{P}$ to account for large deformations, the constitutive models (15) are now stated in a finite-strain setting as

$$\mathbf{P}_i = \mathbf{P}^p\left(\mathbf{F}_i(\boldsymbol{a}_j);\ \boldsymbol{\psi}_i\right)\ ,\ \text{for } i = 0,\ ...,\ N_\mathrm{p} - 1,\ j = 0,\ 1,\ ...,\ N_\mathrm{I} - 1\,. \tag{30}$$

The theory reported in Section 2 is reformulated in a finite-strain setting in Appendix A.1. As a result, Eq. (21) is modified to

$$\mathbf{F}_\mathrm{A} = \mathbf{F}_\mathrm{M} + \frac{1}{v_\mathrm{A}}\hat{\boldsymbol{a}} \otimes \boldsymbol{N}_\mathrm{A}\,,\ \text{and}\ \mathbf{F}_\mathrm{B} = \mathbf{F}_\mathrm{M} - \frac{1}{1.0 - v_\mathrm{A}}\hat{\boldsymbol{a}} \otimes \boldsymbol{N}_\mathrm{A}\,, \tag{31}$$

while the equilibrium equation on the interface, Eq. (19), becomes

$$\left[\mathbf{P}_\mathrm{A}(\mathbf{F}_\mathrm{A}; \boldsymbol{\psi}_\mathrm{A}) - \mathbf{P}_\mathrm{B}(\mathbf{F}_\mathrm{B}; \boldsymbol{\psi}_\mathrm{B})\right] \cdot \boldsymbol{N}_\mathrm{A} = \mathbf{0}\,, \tag{32}$$

where $\boldsymbol{\psi}_\mathrm{A}$ and $\boldsymbol{\psi}_\mathrm{B}$ are respectively the sets of internal variables of phases "A" and "B". These sets of internal variables at a node N_l^k with $l = 0,\ 1,\ ...,\ L-1$ and $k = 0,\ 1,\ ...,\ \left(2^l - 1\right)$ gather recursively the sets of internal variables at the nodes N_{l+1}^{2k} and N_{l+1}^{2k+1} up to reaching the material nodes at the level L for which the internal variables are $\boldsymbol{\psi}_i$ used in the constitutive models (30).

The equilibrium equations need to be solved iteratively at all the interaction interfaces of the IB-DMN. This detailed resolution process in the non-linear finite-strain setting is provided in Appendix A.2.

3.4. Application on a unidirectional (UD) fibre-reinforced matrix composite

In this section, in order to motivate the use of the IB-DMN as a surrogate model, and the further development of a stochastic IB-DMN, we discuss on the accuracy reached by the presented deterministic IB-DMN trained with linear data when predicting non-linear responses. To this end, we consider successively different non-statistically representative volume elements of different volume fractions of UD composites, and train successively three deterministic IB-DMNs of different levels for each of them.

3.4.1. Definition of the non-statistically representative volume elements

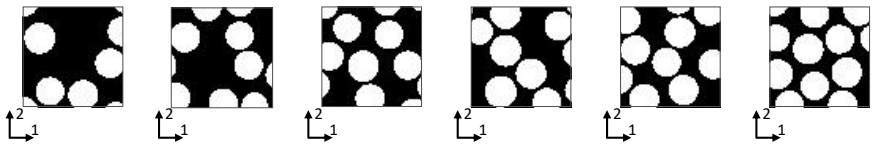

(a) Micro-structure 1 (b) Micro-structure 2 (c) Micro-structure 3 (d) Micro-structure 4 (e) Micro-structure 5 (f) Micro-structure 6

Figure 4: Images of six non-statistically representative volume elements of different volume fractions: (a) $v_{\mathrm{I}} = 0.34$; (b) $v_{\mathrm{I}} = 0.38$; (c) $v_{\mathrm{I}} = 0.45$; (d) $v_{\mathrm{I}} = 0.47$; (e) $v_{\mathrm{I}} = 0.52$; and (f) $v_{\mathrm{I}} = 0.58$.

The micro-structure of the UD fibre-reinforced matrix composite is represented by non-statistically representative volume elements of different volume fractions of size $20\,\mu\mathrm{m} \times 20\,\mu\mathrm{m}$, which are generated to capture the material inherent micro-structural features extracted from SEM images following the approach reported in [55]. Six non-statistically representative volume elements of different volume fractions ranging from 0.34 to 0.58, are illustrated in Fig. 4.

The matrix is modeled as an isotropic material characterised by a Young's modulus E_0 and a Poisson's ratio ν_0 and obeys a finite-strain J_2 elasto-plastic constitutive model [56] as summarised in Appendix B. With an initial yield stress τ_{y}^0, the plastic deformation follows a linear isotropic hardening law, with the von Mises stress criterion reading

$$f = \tau_{\mathrm{eq}} - \tau_{\mathrm{y}}^0 - h\gamma \leq 0\,, \tag{33}$$

where γ is the equivalent plastic strain and h is a material hardening constant.

The transverse isotropic fibres are defined by five material parameters, two Young's moduli $E_{\mathrm{I}}^{\mathrm{T}}$ and $E_{\mathrm{I}}^{\mathrm{L}}$, respectively for the transverse and longitudinal directions, the major and transverse Poisson's ratios $\nu_{\mathrm{I}}^{\mathrm{LT}}$ and $\nu_{\mathrm{I}}^{\mathrm{TT}}$, and the shear modulus $G_{\mathrm{I}}^{\mathrm{LT}}$.

3.4.2. Elastic training of the IB-DMN

The deterministic IB-DMNs are trained independently, each of them corresponding to a non-statistically representative volume element of a given volume fraction. The training data are obtained from direct computational homogenisation applied on the corresponding mesoscopic non-statistically representative volume elements with periodical boundary conditions [57]. Only the elasticity tensor is extracted as data set.

For each non-statistically representative volume element, and thus for the training of the corresponding deterministic IB-DMNs, in order for the topological parameters to be representative of solely the micro-structure organisation and independent of the phases material response, hence allowing for the non-linear simulations in the on-line stage, the material parameters of both phases are randomly generated for each

Table 2: Uniform distribution ranges of material properties with $E_0 = 1.0$.

ν_0	$\log E_{\mathrm{I}}^{\mathrm{T}}$	$E_{\mathrm{I}}^{\mathrm{L}}$	$\nu_{\mathrm{I}}^{\mathrm{LT}}$, $\nu_{\mathrm{I}}^{\mathrm{TT}}$	$G_{\mathrm{I}}^{\mathrm{LT}}$
[0.05, 0.49]	[−2, 3]	$[E_{\mathrm{I}}^{\mathrm{T}}, 25E_{\mathrm{I}}^{\mathrm{T}}]$	[0.05, 0.49]	$[0.5E_{\mathrm{I}}^{\mathrm{T}}, 1.5E_{\mathrm{I}}^{\mathrm{T}}]$

homogenisation data, following independent and conditionally uniform random distributions. Therefore, a set of n homogenised elasticity tensors is generated for each non-statistically representative volume element, each of them corresponding to a different realisation of the elastic properties. In practice $E_0 = 1.0$ is held constant, while the remaining parameters are randomly picked from the ranges provided in Table 2. We note that the elasticity tensors of both the matrix and fibre phases, $\mathbf{C}_0$ and $\mathbf{C}_\mathrm{I}$, can directly be evaluated from these material parameters. Ten sets of random material parameters, $n = 10$ in Eq. (29), are used for each non-statistically representative volume element. The effect of the size of the training data set is studied in Appendix C.1, where it is seen that going beyond $n = 10$ does not improve the predictions. Computational homogenisation then provides the homogenised elasticity tensors, $\hat{\mathbf{C}}_\mathrm{M}\left(\mathbf{C}_0^s, \mathbf{C}_\mathrm{I}^s\right)$, $s = 1, ..., 10$, for each given non-statistically representative volume element and for each realisation of the random material parameters.

For each non-statistically representative volume element illustrated in Fig. 4, three deterministic DMNs of levels $L = 4$, 5 and 6 are successively trained until the loss (29) reaches a value lower than 0.01. It is important to note that the fibre volume fraction is implicitly represented by the parameters v_A of each $\mathcal{G}^2\left(\mathrm{N}_l^k\right)$, where $l = 0$, 1, ..., $L-1$ and $k = 0$, 1, ..., $\left(2^l - 1\right)$, as the loss function (29) is employed.

3.4.3. Material properties and loading conditions during the online stage (predictions)

Table 3: Material properties of the composite components.

Property of fibres	Value
Longitudinal Young's modulus E_I^L [GPa]	231.0
Transverse Young's modulus E_I^T [GPa]	12.99
Transverse Poisson's ratio $\nu_\mathrm{I}^\mathrm{TT}$ [-]	0.46
Longitudinal-Transverse Poisson's ratio $\nu_\mathrm{I}^\mathrm{LT}$ [-]	0.3
Longitudinal-Transverse shear modulus G_I^LT [GPa]	11.3
Property of matrix	**Value**
Young's modulus E_0 [GPa]	4.67
Poisson ratio ν_0 [-]	0.39
Initial yield stress τ_y^0 [MPa]	100.0
Hardening modulus h [MPa]	233.4

To test the accuracy and performance of the six (non-statistically representative volume elements) times three (levels) trained IB-DMNs, we consider the material constants of carbon fibre and of the matrix materials reported in Table 3. Following the coordinates system illustrated in Fig. 4, three loading cases are successively applied on each non-statistically representative volume element:

- Uni-axial strain: $F_{ij} = 0$ for $i \neq j$ (i, $j = 1$, 2, 3), $F_{22} = F_{33} = 1.0$ and F_{11} increasing from 1.0 to 1.1;
- In plane uni-axial stress: $F_{33} = 1.0$, $P_{22} = 0.0$ and F_{11} increasing from 1.0 to 1.1;
- In plane shearing: $F_{ii} = 1.0$ for $i = 1$, 2, 3, $F_{12} = F_{21}$ and increasing from 0 to 0.1;

The predictions of the 18 trained IB-DMNs, corresponding to the six non-statistically representative volume elements of different volume fractions and three different levels (4, 5 and 6) for each non-statistically representative volume element, are plotted in Fig. 5 for the three loading cases, uni-axial strain, in-plane uni-axial stress and in plane shearing. The Direct numerical simulation (DNS) results for the non-statistically representative volume elements of different volume fractions are also reported in Fig. 5 as references. In Fig. 5, it can been seen that accurate predictions have been obtained by all the IB-DMNs in the elastic range.

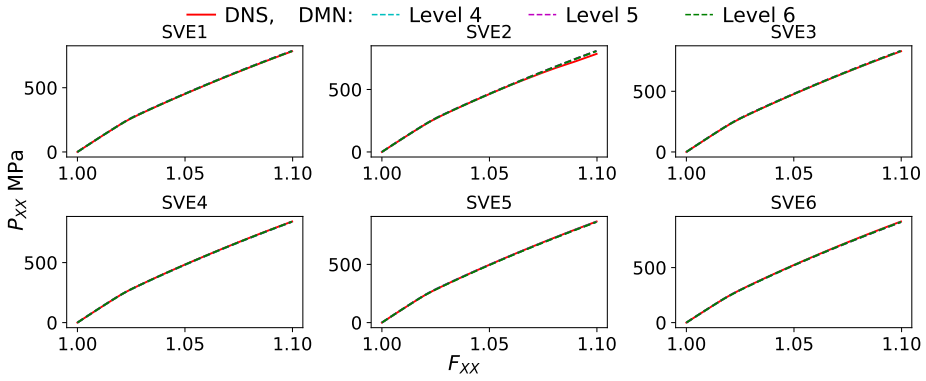

(a) Uni-axial strain

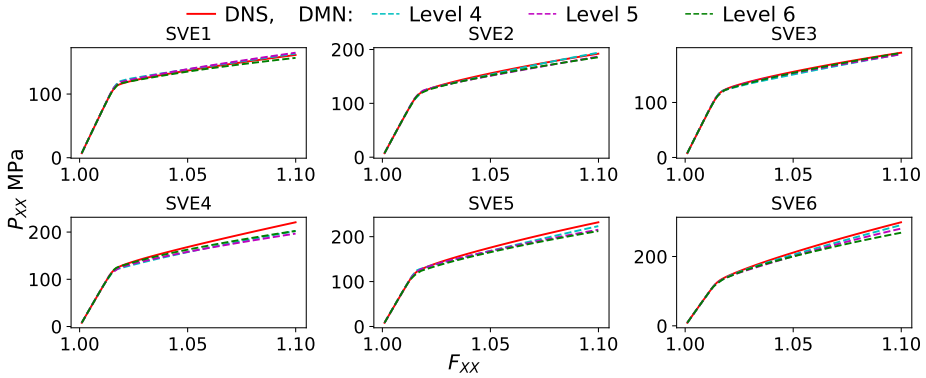

(b) In-plane uni-axial stress

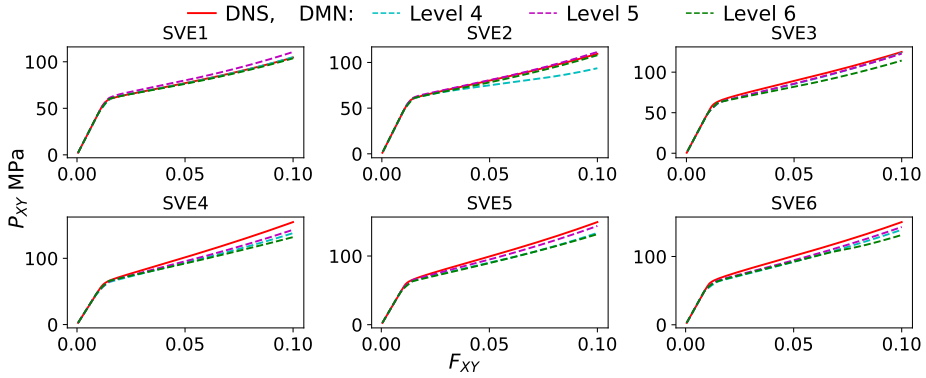

(c) In-plane shearing

Figure 5: The non-linear predictions of the 4-, 5- and 6-level IB-DMNs for the six non-statistically representative volume elements of different volume fractions subjected to the three loading cases: (a) Uni-axial strain; (b) In-plane uni-axial stress; and (c) In-plane shearing. The reference results are obtained from Direct Numerical Simulations (DNSs).

This indicates that the IB-DMNs are well-trained by the elastic training, which is described in Section 3.2.2. However, when the non-statistically representative volume element deformation is out of the elastic range, the IB-DMNs exhibit accurate predictions for the uni-axial strain while for the in-plane uni-axial stress and in-plane shearing loading cases, the DMNs' predictions are less accurate for the higher volume fractions. We observe the same behaviour in an infinitesimal strain setting as reported in Appendix C.2. This observation contrasts with the literature which shows that accurate non-linear predictions can be obtained by DMNs

trained with only linear elastic training. The high accuracy of the non-linear predictions may be attributed to the fact that the meso-scale volume elements used in the literature are close to being Representative Volume Elements (RVEs) and contain more inclusions more evenly distributed within the matrix material, while the micro-structure remains periodic. In contrast, non-statistically representative volume elements are used in the present work, without periodicity constraints in the fibre distribution. Nevertheless, as it was pointed out in [47], a better accuracy can be obtained by considering a training in the non-linear regime.

Since considering a non-linear training would, on the one hand, significantly slow down the training process and, on the other hand, prevent the IB-DMN from being trained with batch data, and thus limit the possibility to develop the stochastic IB-DMN in the next Section 4, in this paper we restrict ourselves to the linear training. Indeed, although less accurate predictions were observed for some loading cases of some non-statistically representative volume elements, it could be seen that all the IB-DMNs still effectively capture the overall trends in the response of the non-statistically representative volume elements. Besides, as it will be shown in the next Section 4, the variability observed with direct numerical simulations on different micro-structure realisations can be reproduced by developing such a stochastic IB-DMN. This motivates building and using directly stochastic IB-DMNs instead of Stochastic Volume Elements (SVEs) to improve computational efficiency in stochastic multi-scale analyses.

4. Stochastic IB-DMN

In this section, building on the IB-DMN structure described in Section 3.2, we develop a stochastic Interaction-Based Deep Material Network, by decoupling the topology parameters of the IB-DMN from the phase volume fraction v_{I}. With the proposed approach, the phase volume fraction becomes an input variable of the IB-DMN and the remaining IB-DMN parameters describe solely the organisation of the micro-structure, allowing the introduction of randomness into the parameters of the IB-DMN.

4.1. Reformulating the topological parameters of the stochastic IB-DMN

In order to introduce randomness into the IB-DMN, the topological parameters are reformulated in order to decouple the volume fraction of the phases from the other IB-DMN's topological parameters for a multi-level two-phase interaction, see Section 3.2. The extension to a multiple-phase material being straightforward.

4.1.1. Outward unit normal $\boldsymbol{N}_A$ of each node of a two-phase interaction

Considering the node N_l^k, $l = 0, 1, ..., L$ and $k = 0, 1, ..., \left(2^l - 1\right)$, since a normal vector has a unit length, it is convenient to express the normal $\boldsymbol{N}_{\mathrm{A}}\left(\mathrm{N}_l^k\right)$ using angular parameters, such as angles $\theta_1\left(\mathrm{N}_l^k\right)$ and $\theta_2\left(\mathrm{N}_l^k\right)$ in a 3D space. This leads to

$$\begin{aligned} \boldsymbol{N}_{\mathrm{A}}\left(\mathrm{N}_l^k\right) &= \left[\cos(\theta_2)\sin\left(\theta_1\right), \cos\left(\theta_2\right)\cos\left(\theta_1\right), \sin\left(\theta_2\right)\right]^{\mathrm{T}}, \\ &\quad \text{with } \theta_1 \in [0,\, 2\pi)\,,\ \theta_2 \in [0,\, \pi)\,, \end{aligned} \tag{34}$$

where we omit the reference to $\left(\mathrm{N}_l^k\right)$ for the two angles for conciseness. The two angular parameters are substituted by $\underline{\mathbf{w}}_{\mathrm{n}}\left(\mathrm{N}_l^k\right) = \left[\mathsf{w}_{\theta_1}\left(\mathrm{N}_l^k\right), \mathsf{w}_{\theta_2}\left(\mathrm{N}_l^k\right)\right]^{\mathrm{T}}$ with

$$\theta_1 = 2\pi\mathsf{w}_{\theta_1}\left(\mathrm{N}_l^k\right), \quad \text{and} \quad \theta_2 = \pi\mathsf{w}_{\theta_2}\left(\mathrm{N}_l^k\right), \tag{35}$$

where $\mathsf{w}_{\theta_1}\left(\mathrm{N}_l^k\right) \in [0,\, 1)$ and $\mathsf{w}_{\theta_2}\left(\mathrm{N}_l^k\right) \in [0, 1\,)$. Equations (34) and (35) establish a one-to-one mapping from $\underline{\mathbf{w}}_{\mathrm{n}}\left(\mathrm{N}_l^k\right)$ to $\boldsymbol{N}_{\mathrm{A}}\left(\mathrm{N}_l^k\right)$. Therefore, we can use $\underline{\mathbf{w}}_{\mathrm{n}}\left(\mathrm{N}_l^k\right) \in [0, 1) \times [0, 1)$ as the parameters for the outward unit normal $\boldsymbol{N}_{\mathrm{A}}\left(\mathrm{N}_l^k\right)$. For a 2D case, only one parameter, $\underline{\mathbf{w}}_{\mathrm{n}}\left(\mathrm{N}_l^k\right) = \left[\mathsf{w}_{\theta_1}\left(\mathrm{N}_l^k\right)\right]$, is needed, and the normal reads $\boldsymbol{N}_{\mathrm{A}}\left(\mathrm{N}_l^k\right) = \left[\sin\left(\theta_1\right), \cos\left(\theta_1\right)\right]^{\mathrm{T}}$.

4.1.2. Volume fraction v_A of each node

For a two-phase heterogeneous material, if the volume fraction of the phase "I" is known and denoted by v_{I}, the volume fraction of the other phase is given by $v_0 = 1.0 - v_{\mathrm{I}}$. Based on the adopted topological parameters, the corresponding nodes are categorized into two types, marked respectively by "green" and "yellow" colours in Fig. 3, for nodes at level $L-1$ and at level $l < L-1$, respectively. The volume fractions for these different nodes are parameterised as follows:

- Composite "yellow" Node at level $l = 0$
  Since the volume fraction v_{I} of the phase "I" is known, v_{I} is an input at the top level ($l = 0$). The volume fraction of the other phase reads $v_0 = 1.0 - v_{\mathrm{I}}$. We thus define the phase volume fraction at this top node as $v_{\mathrm{I}}\left(\mathrm{N}_0^0\right) = v_{\mathrm{I}}$. We define the partition parameters $\underline{\mathbf{w}}_{\mathrm{v}}\left(\mathrm{N}_0^0\right) = \left[\mathsf{w}_{\mathrm{v0}}\left(\mathrm{N}_0^0\right), \mathsf{w}_{\mathrm{vI}}\left(\mathrm{N}_0^0\right)\right]^{\mathrm{T}}$, where $\mathsf{w}_{\mathrm{v0}}\left(\mathrm{N}_0^0\right)$ and $\mathsf{w}_{\mathrm{vI}}\left(\mathrm{N}_0^0\right)$ are both in the range (0, 1), to evaluate the volume fraction v_{A}, *i.e.* the contribution of the node N_1^0 to the composite node N_0^0, following

$$v_{\mathrm{A}}\left(\mathrm{N}_0^0\right) = \mathsf{w}_{\mathrm{v0}}\left(\mathrm{N}_0^0\right) v_0\left(\mathrm{N}_0^0\right) + \mathsf{w}_{\mathrm{vI}}\left(\mathrm{N}_0^0\right) v_{\mathrm{I}}\left(\mathrm{N}_0^0\right) = \mathsf{w}_{\mathrm{v0}}\left(\mathrm{N}_0^0\right) v_0 + \mathsf{w}_{\mathrm{vI}}\left(\mathrm{N}_0^0\right) v_{\mathrm{I}}\,, \tag{36}$$

  and $v_{\mathrm{B}}\left(\mathrm{N}_0^0\right) = 1.0 - v_{\mathrm{A}}\left(\mathrm{N}_0^0\right)$. The volume fractions of the phase "I" at the two nodes at level $l = 1$, see Fig. 3(b), are then evaluated respectively by

$$v_{\mathrm{I}}\left(\mathrm{N}_1^0\right) = \frac{\mathsf{w}_{\mathrm{vI}}\left(\mathrm{N}_0^0\right) v_{\mathrm{I}}\left(\mathrm{N}_0^0\right)}{v_{\mathrm{A}}\left(\mathrm{N}_0^0\right)} \quad \text{and} \quad v_{\mathrm{I}}\left(\mathrm{N}_1^1\right) = \frac{\left(1.0 - \mathsf{w}_{\mathrm{vI}}\left(\mathrm{N}_0^0\right)\right) v_{\mathrm{I}}\left(\mathrm{N}_0^0\right)}{v_{\mathrm{B}}\left(\mathrm{N}_0^0\right)}\,. \tag{37}$$

  Thus, the parameter $\underline{\mathbf{w}}_{\mathrm{v}}\left(\mathrm{N}_0^0\right) = \left[\mathsf{w}_{\mathrm{v0}}\left(\mathrm{N}_0^0\right), \mathsf{w}_{\mathrm{vI}}\left(\mathrm{N}_0^0\right)\right]^{\mathrm{T}}$ also defines the topology parameters for this node.

- Composite "yellow" Node at level $0 < l < L-1$
  Proceeding recursively, we define the partition parameters at node N_l^k, with $k = 1, ..., \left(2^l - 1\right)$, as $\underline{\mathbf{w}}_{\mathrm{v}}\left(\mathrm{N}_l^k\right) = \left[\mathsf{w}_{\mathrm{v0}}\left(\mathrm{N}_l^k\right), \mathsf{w}_{\mathrm{vI}}\left(\mathrm{N}_l^k\right)\right]^{\mathrm{T}}$, where $\mathsf{w}_{\mathrm{v0}}\left(\mathrm{N}_l^k\right)$ and $\mathsf{w}_{\mathrm{vI}}\left(\mathrm{N}_l^k\right)$ are both in the range (0, 1). Knowing the value $v_{\mathrm{I}}\left(\mathrm{N}_l^k\right)$ from the upper level $l-1$, and thus the value $v_0\left(\mathrm{N}_l^k\right) = 1 - v_{\mathrm{I}}\left(\mathrm{N}_l^k\right)$, the volume fraction $v_{\mathrm{A}}\left(\mathrm{N}_l^k\right)$ follows from

$$v_{\mathrm{A}}\left(\mathrm{N}_l^k\right) = \mathsf{w}_{\mathrm{v0}}\left(\mathrm{N}_l^k\right) v_0\left(\mathrm{N}_l^k\right) + \mathsf{w}_{\mathrm{vI}}\left(\mathrm{N}_l^k\right) v_{\mathrm{I}}\left(\mathrm{N}_l^k\right)\,, \tag{38}$$

  with $v_{\mathrm{B}}\left(\mathrm{N}_l^k\right) = 1.0 - v_{\mathrm{A}}\left(\mathrm{N}_l^k\right)$. The volume fractions of the phase "I" at the two nodes at level $l+1$, see Fig. 3(b), are then evaluated respectively by

$$\begin{aligned} v_{\mathrm{I}}\left(\mathrm{N}_{l+1}^{2k}\right) &= \frac{\mathsf{w}_{\mathrm{vI}}\left(\mathrm{N}_l^k\right) v_{\mathrm{I}}\left(\mathrm{N}_l^k\right)}{v_{\mathrm{A}}\left(\mathrm{N}_l^k\right)} \quad \text{and} \\ v_{\mathrm{I}}\left(\mathrm{N}_{l+1}^{2k+1}\right) &= \frac{\left(1.0 - \mathsf{w}_{\mathrm{vI}}\left(\mathrm{N}_l^k\right)\right) v_{\mathrm{I}}\left(\mathrm{N}_l^k\right)}{v_{\mathrm{B}}\left(\mathrm{N}_l^k\right)}\,. \end{aligned} \tag{39}$$

  Thus, the parameter $\underline{\mathbf{w}}_{\mathrm{v}}\left(\mathrm{N}_l^k\right) = \left[\mathsf{w}_{\mathrm{v0}}\left(\mathrm{N}_l^k\right), \mathsf{w}_{\mathrm{vI}}\left(\mathrm{N}_l^k\right)\right]^{\mathrm{T}}$, where $\mathsf{w}_{\mathrm{v0}}\left(\mathrm{N}_l^k\right)$ and $\mathsf{w}_{\mathrm{vI}}\left(\mathrm{N}_l^k\right)$ are both in the range (0, 1), also defines the topology parameters for this node.

- Basic "green" Node at level $L-1$
  Since the volume fraction $v_{\mathrm{I}}\left(\mathrm{N}_{L-1}^k\right)$ is known directly from the upper level $L-2$, we use directly $v_{\mathrm{A}} = 1.0 - v_{\mathrm{I}}\left(\mathrm{N}_{L-1}^k\right)$ and $v_{\mathrm{B}} = v_{\mathrm{I}}\left(\mathrm{N}_{L-1}^k\right)$. No extra parameter is needed for this node.

4.2. Trainable topological parameters of the IB-DMN

According to the description in Sections 4.1.1 and 4.1.2, the components of both parameters $\underline{\mathbf{w}}_{\mathrm{n}}\left(\mathrm{N}_l^k\right)$ and $\underline{\mathbf{w}}_{\mathrm{v}}\left(\mathrm{N}_l^k\right)$ are bounded between 0 and 1. Therefore, a sigmoid function, $\sigma(x) = \frac{1}{1+\mathrm{e}^{-x}}$, is used in order to ensure that the values remain within these bounds, since its output aligns with the parameters range. We thus redefine the topological parameters of the IB-DMN, such that

$$\underline{\mathbf{w}}_{\mathrm{n}}\left(\mathrm{N}_l^k\right) = \sigma\left(\mathcal{T}_{\mathrm{n}}\left(\mathrm{N}_l^k\right)\right) \text{ and } \underline{\mathbf{w}}_{\mathrm{v}}\left(\mathrm{N}_l^k\right) = \sigma\left(\mathcal{T}_{\mathrm{v}}\left(\mathrm{N}_l^k\right)\right) , \tag{40}$$

where $\mathcal{T}_{\mathrm{n}}\left(\mathrm{N}_l^k\right)$ and $\mathcal{T}_{\mathrm{v}}\left(\mathrm{N}_l^k\right)$ are unbounded values and are determined through the training process. Equation (40) excludes the possibility for $\underline{\mathbf{w}}_{\mathrm{n}}\left(\mathrm{N}_l^k\right)$ of being exactly zero, but it can be infinitesimally close to 0.

Using the trainable topological parameters, $\mathcal{T}_{\mathrm{n}}\left(\mathrm{N}_l^k\right)$ and $\mathcal{T}_{\mathrm{v}}\left(\mathrm{N}_l^k\right)$, the two-phase interaction function, "FUN()" defined in Table 1, is modified correspondingly and presented in Table 4. The homogenised elasticity tensor now reads

$$\mathbf{C}_{\mathrm{M}} = \mathrm{FUN}\left(l=0,\, \mathbf{C}_0,\, \mathbf{C}_{\mathrm{I}},\, v_{\mathrm{I}}\left(\mathrm{N}_0^0\right),\, \mathcal{T}_{\mathrm{n}}\left(\mathrm{N}_0^0\right),\, \mathcal{T}_{\mathrm{v}}\left(\mathrm{N}_0^0\right)\right) , \tag{41}$$

where $v_{\mathrm{I}}(\mathrm{N}_0^0) = v_{\mathrm{I}}$ is the volume fraction of phase "I" of the considered heterogeneous material.

Table 4: Two-phase interaction function using the topological parameters $\underline{\mathcal{T}}_{\mathrm{n}}$ and $\underline{\mathcal{T}}_{\mathrm{v}}$

FUN $\left(l,\, \mathbf{C}_0,\, \mathbf{C}_{\mathrm{I}},\, v_{\mathrm{I}}\left(\mathrm{N}_l^k\right),\, \mathcal{T}_{\mathrm{n}}\left(\mathrm{N}_l^k\right),\, \mathcal{T}_{\mathrm{v}}\left(\mathrm{N}_l^k\right)\right)$:

- $\underline{\mathbf{w}}_{\mathrm{n}}\left(\mathrm{N}_l^k\right) = \sigma\left(\mathcal{T}_{\mathrm{n}}\left(\mathrm{N}_l^k\right)\right)$, compute $\boldsymbol{N}_{\mathrm{A}}\left(\mathrm{N}_l^k\right)$ using Eqs. (34) and (35);
- If: $l < L-1$:
  - $\underline{\mathbf{w}}_{\mathrm{v}}\left(\mathrm{N}_l^k\right) = \sigma\left(\mathcal{T}_{\mathrm{v}}\left(\mathrm{N}_l^k\right)\right)$, compute $v_{\mathrm{A}}\left(\mathrm{N}_l^k\right)$ using Eq. (38);
  - Compute $v_{\mathrm{I}}\left(\mathrm{N}_{l+1}^{2k}\right)$ and $v_{\mathrm{I}}\left(\mathrm{N}_{l+1}^{2k+1}\right)$ using Eq. (39);
  - $\mathbf{C}_{\mathrm{A}} = \mathrm{FUN}\left(l+1,\, \mathbf{C}_0,\, \mathbf{C}_{\mathrm{I}},\, v_{\mathrm{I}}(\mathrm{N}_{l+1}^{2k}),\, \mathcal{T}_{\mathrm{n}}\left(\mathrm{N}_{l+1}^{2k}\right),\, \mathcal{T}_{\mathrm{v}}\left(\mathrm{N}_{l+1}^{2k}\right)\right)$;
  - $\mathbf{C}_{\mathrm{B}} = \mathrm{FUN}\left(l+1,\, \mathbf{C}_0,\, \mathbf{C}_{\mathrm{I}},\, v_{\mathrm{I}}\left(\mathrm{N}_{l+1}^{2k+1}\right),\, \mathcal{T}_{\mathrm{n}}\left(\mathrm{N}_{l+1}^{2k+1}\right),\, \mathcal{T}_{\mathrm{v}}\left(\mathrm{N}_{l+1}^{2k+1}\right)\right)$;
- Else:
  - For a two-phase material $\mathbf{C}_{\mathrm{A}} = \mathbf{C}_0$, $\mathbf{C}_{\mathrm{B}} = \mathbf{C}_{\mathrm{I}}$ and $v_{\mathrm{A}} = 1.0 - v_{\mathrm{I}}\left(\mathrm{N}_{L-1}^k\right)$;
- Compute $\mathbf{C}_{\mathrm{M}}$ using Eqs. (25) and (27)
- Return $\mathbf{C}_{\mathrm{M}}$

4.3. Random topological parameters, $\mathcal{T}_n\left(N_l^k\right)$ and $\mathcal{T}_v\left(N_l^k\right)$

The uncertainty in the response of a SVE arises from its random micro-structure, which includes the random phase volume fraction v_{I} and the arrangement or distributions of the different phases. From Eq. (41), it can be observed that the variation in the topological parameters, $\mathcal{T}_{\mathrm{v}}\left(\mathrm{N}_l^k\right)$, does not affect the consistency of the volume fraction of phases in the heterogeneous material. Thus, we can decouple the two sources of uncertainty in a SVE. The random phase volume fraction v_{I} of a SVE is easily generated by following a given distribution, while we use the random topological parameters, $\mathcal{T}_{\mathrm{n}}\left(\mathrm{N}_l^k\right)$ and $\mathcal{T}_{\mathrm{v}}\left(\mathrm{N}_l^k\right)$, to mimic the uncertainty in the spatial organisation of the phases in a SVE.

To define the stochastic IB-DMN, a reference IB-DMN with topological parameters $\tilde{\mathcal{T}}_{\mathrm{n}}\left(\mathrm{N}_l^k\right)$ and $\tilde{\mathcal{T}}_{\mathrm{v}}\left(\mathrm{N}_l^k\right)$ is used. The random topological parameters, $\mathcal{T}_{\mathrm{n}}\left(\mathrm{N}_l^k\right)$ and $\mathcal{T}_{\mathrm{v}}\left(\mathrm{N}_l^k\right)$, are obtained by introducing random perturbations to those of the reference IB-DMN, following

$$\mathcal{T}_*\left(\mathrm{N}_l^k\right) = (1.0 + \boldsymbol{\xi}) \odot \tilde{\mathcal{T}}_*\left(\mathrm{N}_l^k\right) , \tag{42}$$

where $\mathcal{T}_*\left(\mathrm{N}_l^k\right)$ refers to either $\mathcal{T}_{\mathrm{n}}\left(\mathrm{N}_l^k\right)$ or $\mathcal{T}_{\mathrm{v}}\left(\mathrm{N}_l^k\right)$, $\boldsymbol{\xi}$ is a random vector of the same dimension as $\mathcal{T}_*$, and $\odot$ denotes the element-wise multiplication operator. To keep it simple, it is assumed that all the elements of the random vector $\boldsymbol{\xi}$ are independent random variables following the same distribution. From the expression of Eq. (42), it can be seen that a bounded distribution centered around zero would be a favorable choice. Among the classic distributions, the Beta distribution, Beta(α, β), is bounded between 0 and 1 and centered at 0.5. Thus, using a randomly generated variable χ following $\chi \sim \mathrm{Beta}(\alpha, \beta)$, an element of $\boldsymbol{\xi}$ is given by

$$\xi = 2b(\chi - 0.5) , \tag{43}$$

where, ξ is bounded in the range $(-b, b)$, while its variance is controlled by the range parameter b and the Beta distribution parameters α and β. It needs to be noted that in all generality, $\alpha \neq \beta$ can be used, but also different α and β values can be applied to the different groups, $\mathcal{T}_{\mathrm{n}}\left(\mathrm{N}_l^k\right)$ and $\mathcal{T}_{\mathrm{v}}\left(\mathrm{N}_l^k\right)$, of the topological parameters, such as using $\chi_{\mathrm{n}} \sim \mathrm{Beta}(\alpha_{\mathrm{n}}, \beta_{\mathrm{n}})$ and $\chi_{\mathrm{v}} \sim \mathrm{Beta}(\alpha_{\mathrm{v}}, \beta_{\mathrm{v}})$ to generate ξ_{n} for $\mathcal{T}_{\mathrm{n}}\left(\mathrm{N}_l^k\right)$ and ξ_{v} for $\mathcal{T}_{\mathrm{v}}\left(\mathrm{N}_l^k\right)$, respectively.

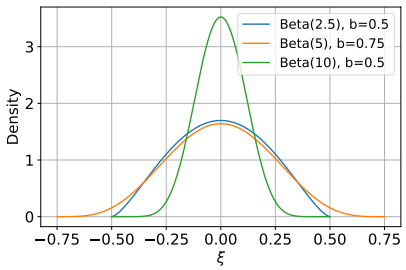

Figure 6: Probability density function of ξ.

Nevertheless, for simplicity, we use $\alpha = \beta$ and, in this case, we write the Beta distribution as Beta(α). Using different parameters α and b, the distribution of ξ is illustrated in Fig. 6.

However, the chosen values of parameters α and b need to preserve the stochastic content of the non-linear responses of the SVEs, as it will be discussed in Section 5.

4.4. The training of the reference IB-DMN

In this Section, we detail the methodology to train the reference IB-DMN independently to the volume fraction v_{I}, *i.e.* to determine the topological parameters, $\tilde{\mathcal{T}}_{\mathrm{n}}\left(\mathrm{N}_l^k\right)$ and $\tilde{\mathcal{T}}_{\mathrm{v}}\left(\mathrm{N}_l^k\right)$ that will serve as a basis for the stochastic IB-DMN so that the variation of the volume fraction and of the fibre distribution can be accounted for with the method described in Section 4.3. Toward this end, we generate several SVE realisations following the methodology described in [55]. The fibre volume fraction, v_{I}, in the SVEs varies from 0.25 to 0.6, with 60 SVE realisations generated per 0.01-increment in the fibre volume fraction.

The training data is generated according to the description provided in Section 3.4.2, with one set of random material parameters being applied for each SVE. We note that the training data set thus corresponds to different SVE realisations of different fibre volume fractions in the range 0.25 to 0.6, motivating the training of the reference IB-DMN to be achieved in the linear range.

For the trainable topological parameters of the reference IB-DMN, we use $\underline{\tilde{\mathcal{T}}}_{\rm n}$ to represent the aggregate of $\tilde{\mathcal{T}}_{\rm n}\left(\mathrm{N}_l^k\right)$, $l = 0,\, 1,\, ...,\, L-1$ and $k = 0,\, 1,\, ...,\, \left(2^l-1\right)$, and $\underline{\tilde{\mathcal{T}}}_{\rm v}$ for the aggregate of $\tilde{\mathcal{T}}_{\rm v}\left(\mathrm{N}_l^k\right)$, $l = 0,\, 1,\, ...,\, L-2$ and $k = 0,\, 1,\, ...,\, \left(2^l-1\right)$. At the start of training, all elements of the parameters $\underline{\tilde{\mathcal{T}}}_{\rm n}$ and $\underline{\tilde{\mathcal{T}}}_{\rm v}$ are initialised with random values, uniformly distributed in the range $(-0.5,\, 0.5)$. They are then refined through the minimisation of the loss function, which is modified from Eq. (29) as

$$Loss(\hat{\mathbf{C}}_{\rm M}\,,\mathbf{C}_{\rm M}) = \frac{1}{n}\sum_{s=1}^{n}\frac{\|\hat{\mathbf{C}}_{\rm M}(\mathbf{C}_0^s\,,\mathbf{C}_{\rm I}^s) - \mathbf{C}_{\rm M}(\mathbf{C}_0^s\,,\mathbf{C}_{\rm I}^s\,,v_{\rm I}^s;\,\underline{\tilde{\mathcal{T}}}_{\rm n}\,,\underline{\tilde{\mathcal{T}}}_{\rm v})\|}{\|\hat{\mathbf{C}}_{\rm M}(\mathbf{C}_0^s\,,\mathbf{C}_{\rm I}^s)\|}\,, \tag{44}$$

where the training data $\hat{\mathbf{C}}_{\rm M}$ are obtained from the direct finite element simulations on the SVEs, n is the number of data used in the training, and where the elasticity tensors, $\mathbf{C}_{\rm M}$, are obtained through the IB-DMN predictions, Eq. (41).

The reference 4-, 5- and 6-level IB-DMNs have been trained for 5000 epochs with mini-batch data. Each mini-batch consists of 10% of the training data, randomly picked, and is shuffled after every 5 training epochs. The final losses, on all the training data, reached around 0.060 for all the reference of 4-, 5- and 6-level IB-DMNs, see discussion in Section 6.

The "FUN()" function in Table 4, the loss function, Eq. (44), and the training of the IB-DMN were implemented using PyTorch. The "AdamW" algorithm is used to minimise the loss function.

5. Non-Linear response envelope of UD SVEs realisations: stochastic IB-DMNs *vs.* DNS

To test the developed stochastic IB-DMNs in Section 4, the material system detailed in Section 3.4 is considered. According to the results plotted in Fig. 5, we consider the last two loading cases, *i.e.* the in-plane uni-axial stress and shearing conditions, for which the effect of the micro-structure on the non-linear response is more pronounced.

SVEs are generated using the formalism presented in [55]. The fibre volume fraction of the SVEs increases from 0.3 to 0.6, with each 0.05 increment in volume fraction considered as a sub-range. 100 SVEs are generated for each of these sub-ranges of volume fraction. The fibre volume fraction, $v_{\rm I}$, of each SVE realisation is saved and will be used as input for the IB-DMN.

As reference results, direct numerical simulations are conducted in the non-linear range on the generated SVE realisations using periodic boundary conditions: 100, respectively 30, SVEs are simulated under in-plane uni-axial stress, respectively shearing, condition for each sub-range of volume fraction[3]. In the presented approach, in which the randomness is introduced through the topology parameters $\underline{\mathcal{T}}_{\rm n}$ and $\underline{\mathcal{T}}_{\rm v}$, there is no correspondence between one SVE realisation of the DNSs and one IB-DMN realisation: only the statistical content of the responses is compared.

Arbitrary values of the distribution parameters of the stochastic IB-DMNs are first considered to illustrate the ability of the stochastic IB-DMN to serve as a surrogate. The choice of the distribution parameters is then refined in order to capture the statistical content of the SVE responses.

5.1. 4-, 5- and 6-level stochastic IB-DMNs with $\alpha = 2.5$ and $b = 0.5$

The random parameters are generated according to Eqs. (42) and (43) using, at first for illustration purpose, $\chi \sim$ Beta(2.5) and $b = 0.5$ for all the topological parameters of the stochastic IB-DMN, *i.e.* for $\mathcal{T}_{\rm n}\left(\mathrm{N}_l^k\right)$, $l = 0,\, 1,\, ...,\, L-1$ and $k = 0,\, 1,\, ...,\, \left(2^l-1\right)$, and $\mathcal{T}_{\rm v}\left(\mathrm{N}_l^k\right)$, $l = 0,\, 1,\, ...,\, L-2$ and $k = 0,\, 1,\, ...,\, \left(2^l-1\right)$.

For each level of the stochastic IB-DMN, the volume fraction $v_{\rm I}$, obtained from direct finite element simulations, is used as input for the non-linear in-plane uniaxial stress and shearing simulations. The non-linear predictions of the Direct Numerical Simulation (DNS) and of the 4-level, 5-level, and 6-level stochastic

[3]Direct numerical simulation of some SVEs under in-plane shearing can be quite time-consuming.

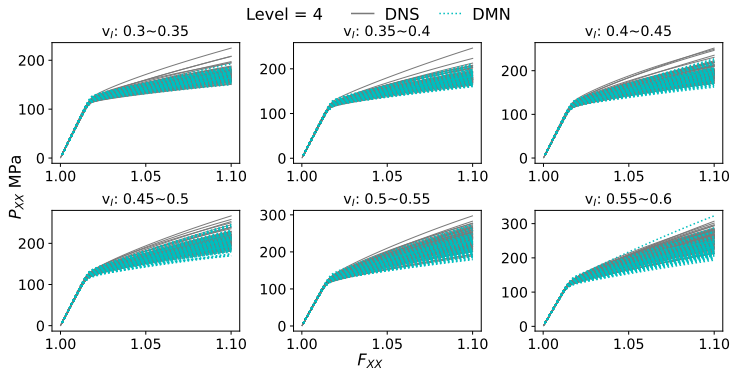

(a)

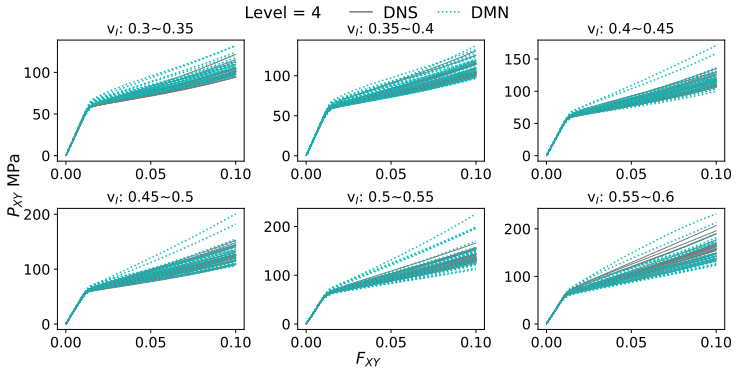

(b)

Figure 7: The non-linear predictions of the 4-level stochastic IB-DMN with $\chi \sim \text{Beta}(2.5)$ and $b = 0.5$ for (a) In-plane uniaxial stress; and (b) In-plane shearing. DNS simulations are also reported for comparison purpose.

IB-DMNs are plotted in Figs. 7, 8, and 9, respectively. It can be observed that the strain-stress curves from DNS are largely captured by those of the stochastic IB-DMNs for both in-plane uniaxial stress and shearing loading conditions. This demonstrates that the stochastic IB-DMN can serve as an effective surrogate of direct numerical simulations conducted on the SVEs.

The Figs. 7, 8, and 9 show no significant effect from the total level of the DMN. However, the computational cost of the 6-level IB-DMN is significantly higher than that of the 4- and 5-level IB-DMNs. Therefore, in the remaining of this paper, we will consider the sole 5-level IB-DMN.

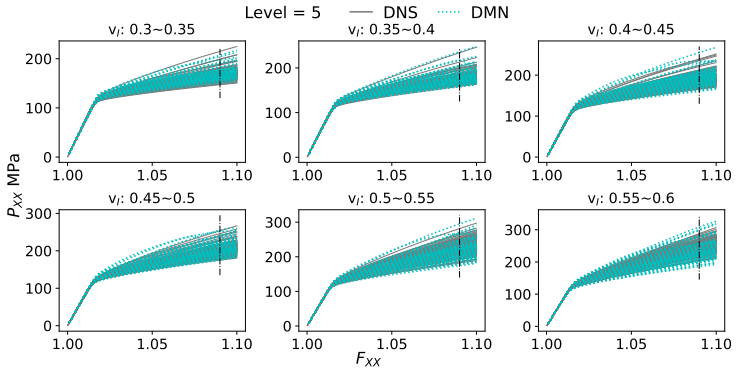

(a)

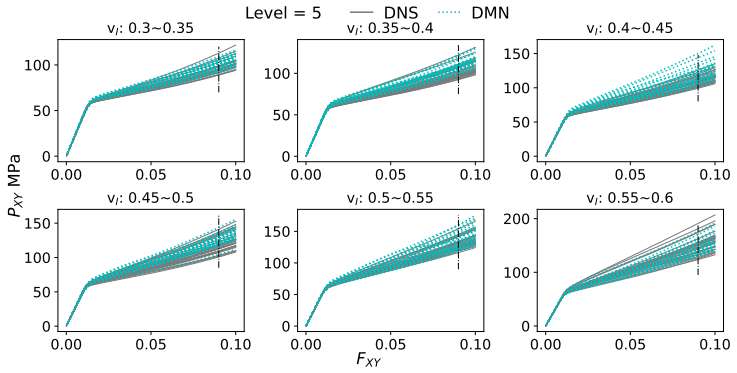

(b)

Figure 8: The non-linear predictions of the 5-level stochastic IB-DMN with $\chi \sim \text{Beta}(2.5)$ and $b = 0.5$ for (a) In-plane uniaxial stress; and (b) In-plane shearing. DNS simulations are also reported for comparison purpose.

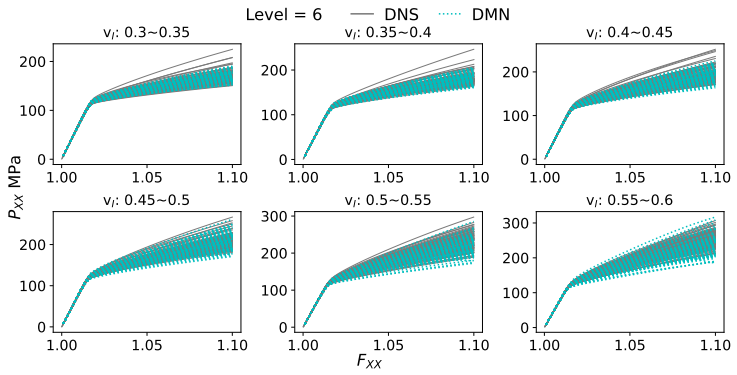

(a)

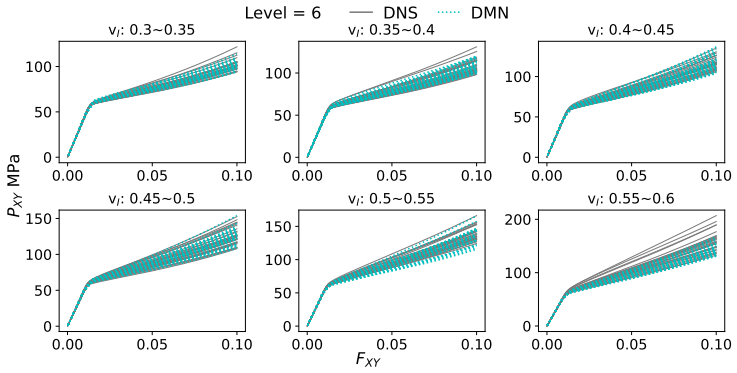

(b)

Figure 9: The non-linear predictions of the 6-level stochastic IB-DMN with $\chi \sim \text{Beta}(2.5)$ and $b = 0.5$ for (a) In-plane uniaxial stress; and (b) In-plane shearing. DNS simulations are also reported for comparison purpose.

5.2. The effect of the distribution parameters α and b

In this Section, different values of the distribution parameters, α and b of Eq. (43), are used in the 5-level stochastic IB-DMN, with the perturbation being applied on all the topological parameters, *i.e.* for $\mathcal{T}_{\mathrm{n}}\left(\mathrm{N}_l^k\right)$, $l = 0, 1, ..., L-1$ and $k = 0, 1, ..., \left(2^l - 1\right)$, and $\mathcal{T}_{\mathrm{v}}\left(\mathrm{N}_l^k\right)$, $l = 0, 1, ..., L-2$ and $k = 0, 1, ..., \left(2^l - 1\right)$.

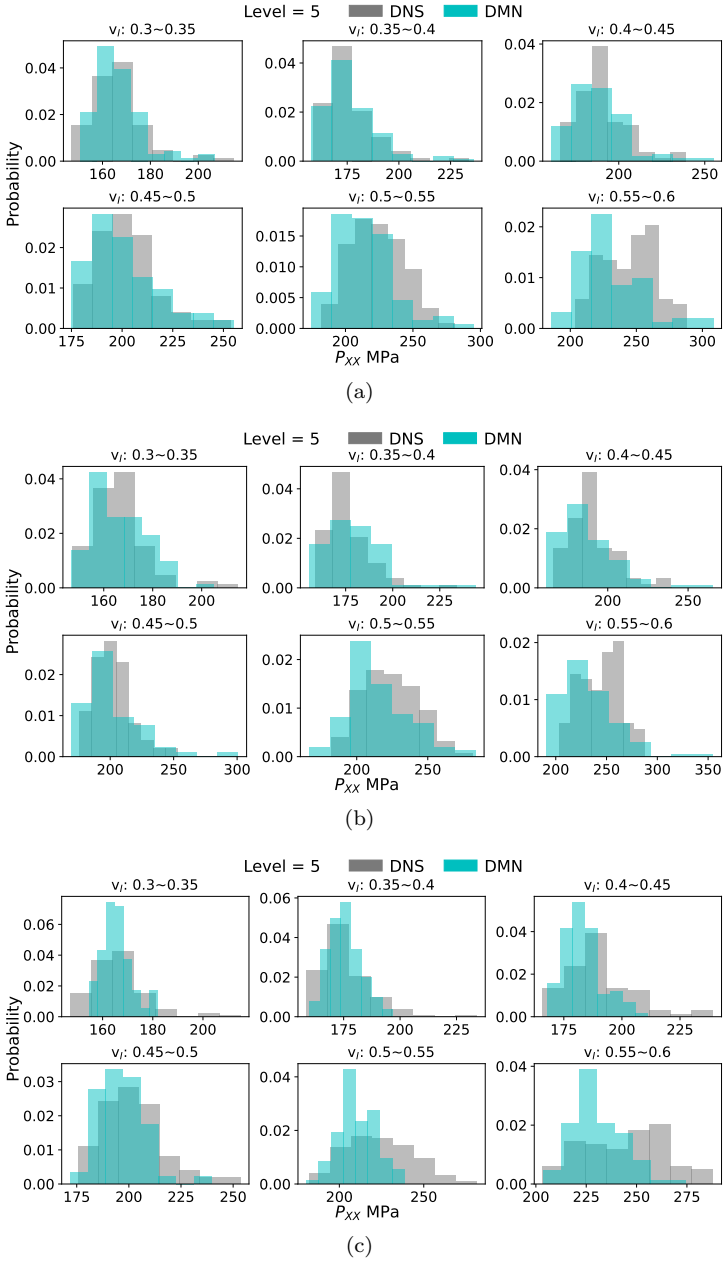

Figure 10: The histograms of the response stress reached at $F_{xx} = 1.09$ for in-plane uni-axial stress loading condition. Comparison of the DNS results with the 5-level stochastic IB-DMN predictions using: (a) $\alpha = 2.5$, $b = 0.5$; (b) $\alpha = 5$, $b = 0.75$; and (c) $\alpha = 10$, $b = 0.5$.

The three sets of parameters used to illustrate the distribution of ξ in Fig. 6, *i.e.* $[\alpha = 2.5, b = 0.5]$, $[\alpha = 5, b = 0.75]$ and $[\alpha = 10, b = 0.5]$, are now successively considered. The histograms of the response

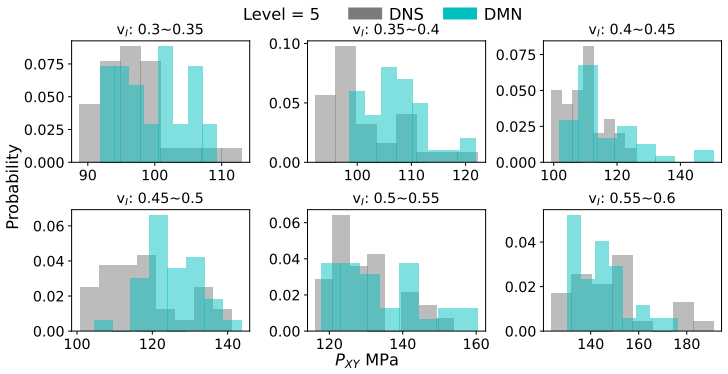

(a)

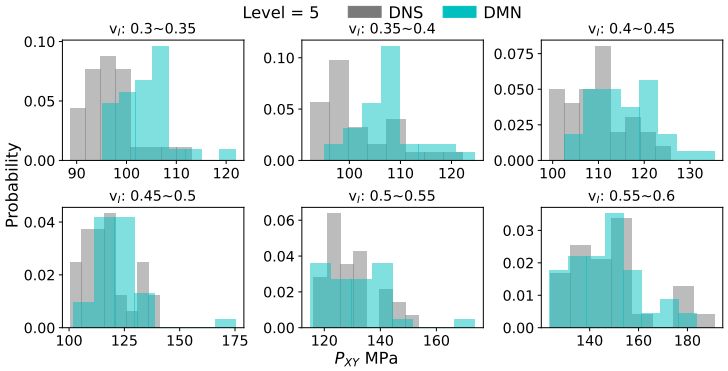

(b)

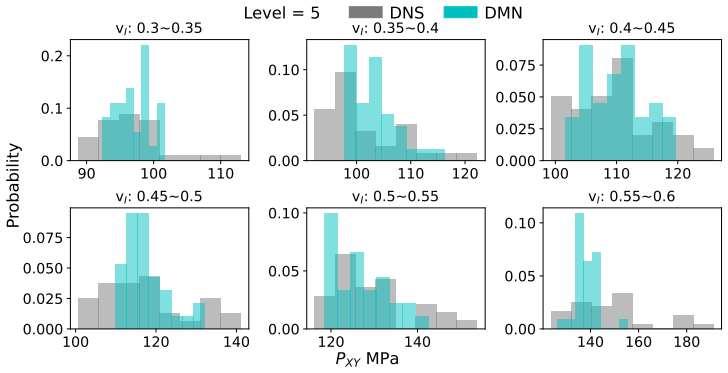

(c)

Figure 11: The histograms of the response stress reached at $F_{xy} = 0.09$ for in-plane shearing loading condition. Comparison of the DNS results with the 5-level stochastic IB-DMN predictions using: (a) $\alpha = 2.5$, $b = 0.5$; (b) $\alpha = 5$, $b = 0.75$; and (c) $\alpha = 10$, $b = 0.5$.

stress reached at $F_{xx} = 1.09$ for the in-plane uni-axial stress loading condition and at $F_{xy} = 0.09$ for the in-plane shearing, as indicated by the black dash-dot lines in Fig. 8, are respectively reported in Figs. 10 and 11 for both the DNSs conducted on the SVE realisations and the stochastic IB-DMN predictions.

In Fig. 6 it is observed that the distributions of the perturbation variable, ξ, are quite similar for the parameter sets $[\alpha = 2.5, b = 0.5]$ and $[\alpha = 5, b = 0.75]$, while using $[\alpha = 10, b = 0.5]$ results in a distribution of ξ with lower variance. Correspondingly, the stochastic IB-DMNs using $[\alpha = 2.5, b = 0.5]$ and $[\alpha = 5, b = 0.75]$ also yield similar variance in the histograms of the response stress, see Figs. 10(a),

10(b), 11(a) and 11(b). Furthermore, a lower variance in the histograms of the response stress is obtained with the stochastic IB-DMN using [$\alpha = 10$, $b = 0.5$], see Figs. 10(c) and 11(c). This indicates that the stochastic response of the IB-DMN is controlled by the distribution of its perturbation variable, ξ, which can be adjusted through the parameters α and β of the Beta distribution, and through the parameter b for the distribution range.

When considering the two different parameters combinations [$\alpha = 2.5$, $b = 0.5$] and [$\alpha = 5$, $b = 0.75$] with the stochastic IB-DMNs, Figs. 10(a), 10(b), 11(a) and 11(b) have shown that the stochastic responses from the DNSs conducted on the SVE realisations are well reproduced. Nevertheless, the distribution parameters α, β and b, should be more rigorously determined based on the stochastic response of the SVEs from DNS results, for instance through Bayesian inference, which is beyond the scope of this work.

5.3. The effect of partially applying the perturbation on the topological parameters of the stochastic IB-DMN

In this section, we still consider the 5-level stochastic IB-DMN with $\alpha = 2.5$ and $b = 0.5$ to define the perturbation variable ξ, Eq. (43). Contrarily to the previous section, instead of applying the perturbation to all the topological parameters, the perturbation is applied to the topological parameters $\tilde{\mathcal{T}}_{\mathrm{n}}\left(\mathrm{N}_l^k\right)$ and $\tilde{\mathcal{T}}_{\mathrm{v}}\left(\mathrm{N}_l^k\right)$ at given levels only, while the remaining parameters remain constant, *i.e.* the same as those in the reference IB-DMN. Four cases are studied:

- Case 1: Perturbation is only applied to all $\tilde{\mathcal{T}}_{\mathrm{n}}\left(\mathrm{N}_l^k\right)$, $l = 0, 1, ..., 4$;
- Case 2: Perturbation is only applied to all $\tilde{\mathcal{T}}_{\mathrm{v}}\left(\mathrm{N}_l^k\right)$, $l = 0, 1, ..., 3$;
- Case 3: Perturbation is applied to $\tilde{\mathcal{T}}_{\mathrm{n}}(\mathrm{N}_{l=4}^k)$ and $\tilde{\mathcal{T}}_{\mathrm{v}}(\mathrm{N}_{l=3}^k)$;
- Case 4: Perturbation is applied to $\tilde{\mathcal{T}}_{\mathrm{n}}(\mathrm{N}_{l=3}^k)$ and $\tilde{\mathcal{T}}_{\mathrm{v}}(\mathrm{N}_{l=2}^k)$;

where $k = 0, ..., 2^l - 1$. Following Section 4.1.1, the topology parameters $\mathcal{T}_{\mathrm{n}}\left(\mathrm{N}_l^k\right)$ related to the normal direction are defined for nodes N_l^k, with $l = 0, 1, ..., L-1$ and $k = 0, 1, ..., \left(2^l - 1\right)$, while, following Section 4.1.2, the topology parameters $\mathcal{T}_{\mathrm{v}}\left(\mathrm{N}_l^k\right)$ related to the volume fraction are only defined on nodes N_l^k, with $l = 0, 1, ..., L-2$ and $k = 0, 1, ..., \left(2^l - 1\right)$, meaning up to one level lower of the tree than for $\mathcal{T}_{\mathrm{n}}\left(\mathrm{N}_l^k\right)$. This explains why the different studied cases discreminate between the higher perturbated level.

The histograms of the response stress reached at $F_{xx} = 1.09$ for the in-plane uni-axial stress loading and at $F_{xy} = 0.09$ for the in-plane shearing loading are plotted in Figs. 12 - 15, respectively for the four cases of partially perturbed topological parameters.

Fig. 12 shows that the stochastic characteristics of the response stress obtained from DNS on SVEs can be reproduced by the stochastic IB-DMN with the case 1 of partially perturbed topological parameters, *i.e.* for which the perturbation is only applied to all $\tilde{\mathcal{T}}_{\mathrm{n}}\left(\mathrm{N}_l^k\right)$. In contrast, Fig. 13 shows that lower variances of the response stress are obtained from the stochastic IB-DMN with the case 2 of partially perturbed topological parameters, *i.e.* for which the perturbation is only applied to all $\tilde{\mathcal{T}}_{\mathrm{v}}\left(\mathrm{N}_l^k\right)$. This suggests that the uncertain non-linear response of the IB-DMN is dominated by the topological parameters $\mathcal{T}_{\mathrm{n}}\left(\mathrm{N}_l^k\right)$, when $\alpha = 2.5$ and $b = 0.5$ are used to define the perturbation variable ξ, Eq. (43).

Comparing the variance of the response stress obtained for the case 3 of partially perturbed topological parameters with the one for the case 4 indicates that the uncertainty of the topological parameters at deeper levels has a more pronounced effect on the non-linear response variability predicted by the stochastic IB-DMN, see Figs. 14 and 15.

From the results plotted in Figs. 12 and 14, we can see that a IB-DMN can be constructed to serve as a surrogate for DNS on SVEs by applying perturbations selectively to its topological parameters.

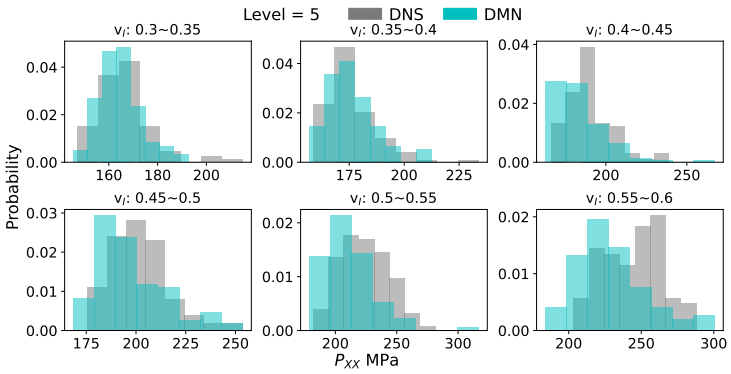

(a)

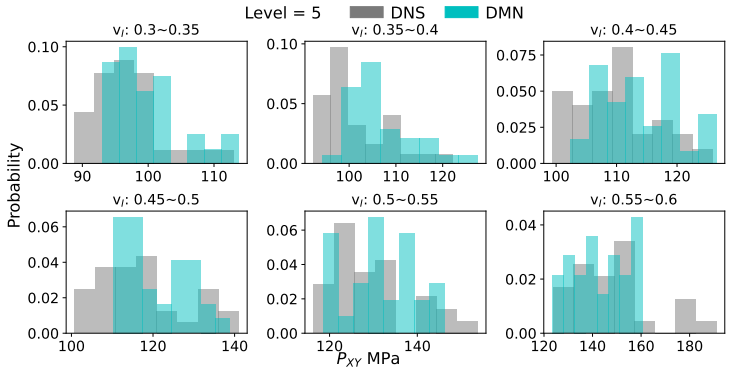

(b)

Figure 12: The histograms of the response stress at (a) $F_{xx} = 1.09$ for in-plane uni-axial stress loading; and (b) $F_{xy} = 0.09$ for in-plane shearing loading conditions. Comparison of the DNS results with the 5-level stochastic IB-DMN predictions with "Case 1" partially perturbed topological parameters.

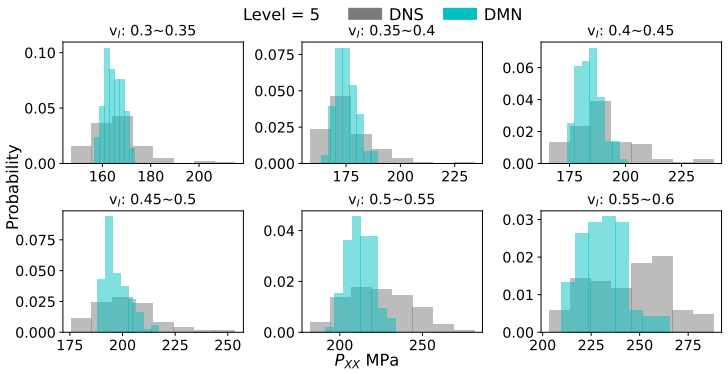

(a)

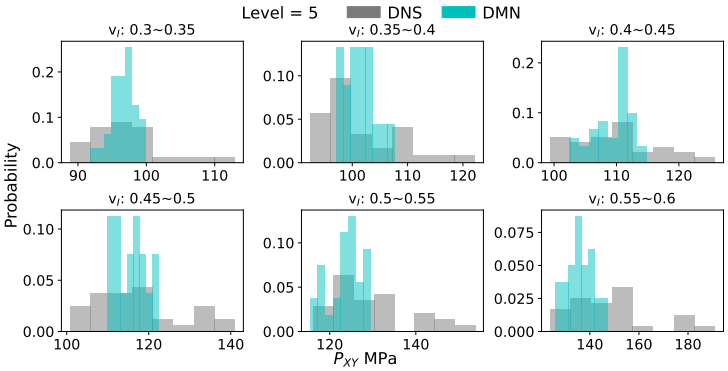

(b)

Figure 13: The histograms of the response stress at (a) $F_{xx} = 1.09$ for in-plane uni-axial stress loading; and (b) $F_{xy} = 0.09$ for in-plane shearing loading conditions. Comparison of the DNS results with the 5-level stochastic IB-DMN predictions with "Case 2" partially perturbed topological parameters.

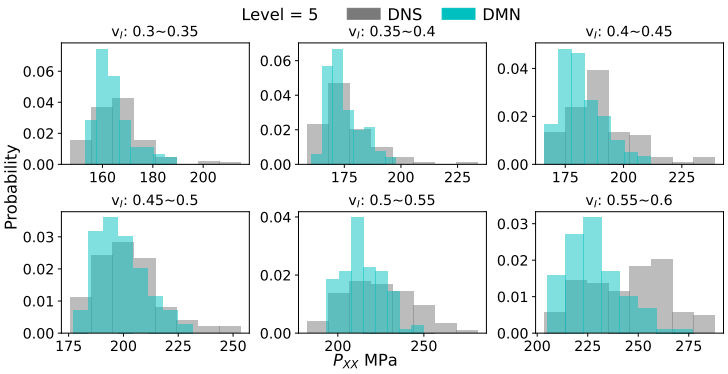

(a)

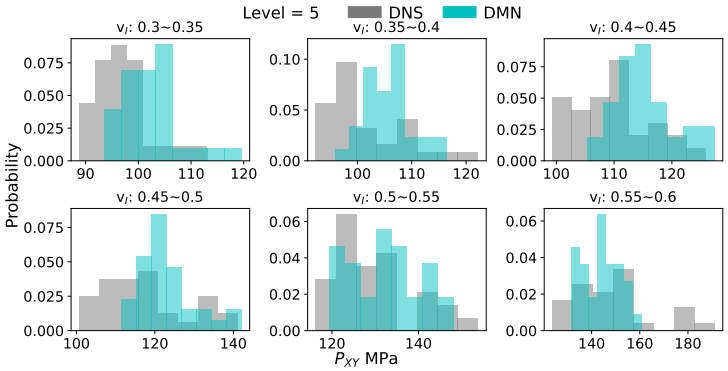

(b)

Figure 14: The histograms of the response stress at (a) $F_{xx} = 1.09$ for in-plane uni-axial stress loading; and (b) $F_{xy} = 0.09$ for in-plane shearing loading conditions. Comparison of the DNS results with the 5-level stochastic IB-DMN predictions with "Case 3" partially perturbed topological parameters.

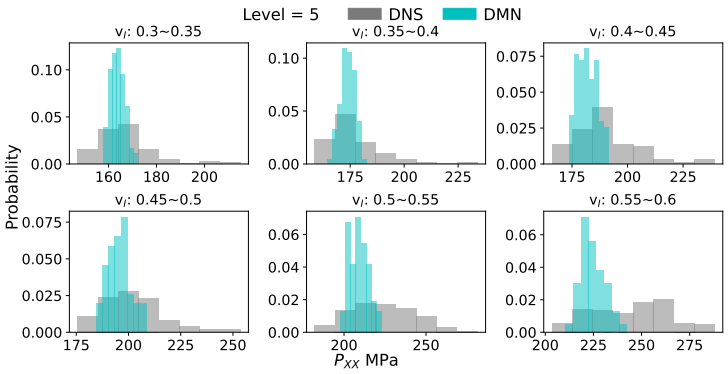

(a)

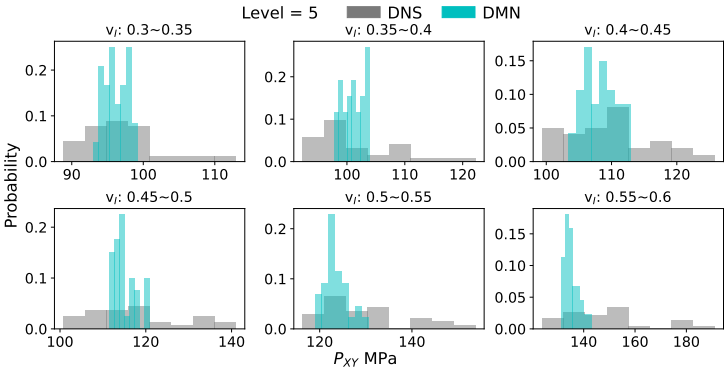

(b)

Figure 15: The histograms of the response stress at (a) $F_{xx} = 1.09$ for in-plane uni-axial stress loading; and (b) $F_{xy} = 0.09$ for in-plane shearing loading conditions. Comparison of the DNS results with the 5-level stochastic IB-DMN predictions with "Case 4" partially perturbed topological parameters.

5.4. Discussion on case 1: Perturbation is only applied to all $\tilde{\mathcal{T}}_n\left(N_l^k\right)$

We consider the case 1 of the previous section and apply the perturbation only to all $\tilde{\mathcal{T}}_{\mathrm{n}}\left(\mathrm{N}_l^k\right)$, $l = 0, 1, ..., 4$. However in this section, $\alpha = 2.5$ and $b = 1.0$ are considered in order to increase the variance of the perturbation variable ξ, Eqs. (43).

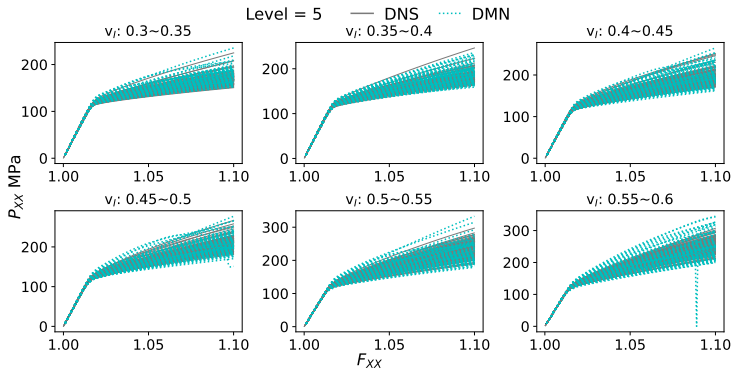

(a)

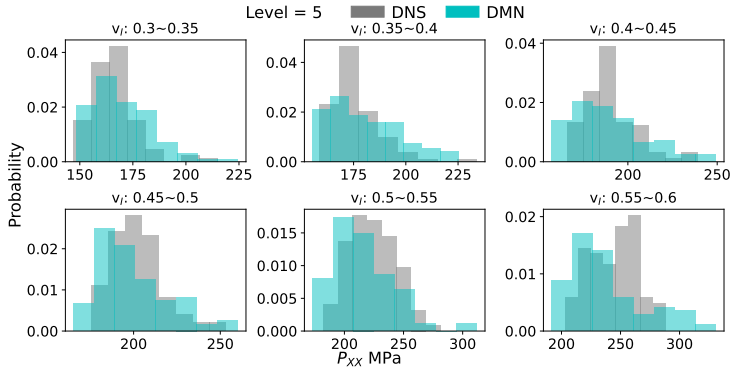

(b)

Figure 16: Comparison of the DNS results with the 5-level stochastic IB-DMN predictions with "Case 1" partially perturbed topological parameters using $\alpha = 2.5$ and $b = 1.0$ for in-plane uni-axial stress loading: (a) The non-linear predictions; and (b) The histograms of the response stress at $F_{xx} = 1.09$.

The stochastic response stress predicted using the 5-level stochastic IB-DMN is reported in Fig. 16(a) for the in-plane uni-axial stress loading condition. Comparing Fig. 16(b) with Fig. 13(a), it can be seen that, when increasing the random perturbation range, the variance of the response stress is increased and approaches those of the DNS. However, at high volume fraction, one IB-DMN realisation exhibited a convergence issue during one step increment (although the simulation did not converge we let the response in the graph for completeness).

6. Computational efficiency of the IB-DMN

Like for any kind of surrogate models, the efficiency of the online simulations of the IB-DMN comes at the cost of the offline stage. The numbers of training and testing data points are listed in Table 5. It takes approximately 25 seconds to generate a single data point, resulting in over 100 hours for the training data generation, while more data are generated for testing purpose. Nevertheless, this data generation time can be easily scaled through parallel computation since they are independent from each others.

Table 5: Computational efficiency of the IB-DMN

Data preparation (off-line stage)			
	Training	Testing	
Data size	16800	24600	
Data generation	116.7h	170.8h	
CPU Time	around 25s per data		

Training time for 5000 epochs (off-line stage)				
DMN		4-Level IB-DMN	5-Level IB-DMN	6-Level IB-DMN
Mini-batch	1680	4.1h	14.2h	23.4h
size	336	1h	2.6h	5.8h

Final loss (off-line stage)			
DMN	4-Level IB-DMN	5-Level IB-DMN	6-Level IB-DMN
Training MRE	0.061	0.061	0.060
Testing MRE	0.047	0.045	0.044

Non-linear simulation time (online stage)				
	DMN			
	4-Level IB-DMN	5-Level IB-DMN	6-Level IB-DMN	DNS
In-plane uni-axial stress	< 1s	< 3s	< 10s	$0.6 \sim > 2$h
In-plane shearing	< 1s	< 3s	< 10s	$3 \sim > 10$h

The training time of the reference IB-DMN, see Section 4.4, depends on the depth of the IB-DMN and of the chosen mini-batch size during training. As shown in Table 5, deeper IB-DMNs require more time to be trained. However, the training time can be reduced by using smaller mini-batch sizes. With data shuffling every 5 epochs, similar accuracy is achieved by the IB-DMNs trained with the two different mini-batch sizes listed in Table 5, while reducing the training time by 4.

The final losses, measured using the Mean Relative Error (MRE) defined in Eq. (44), of the IB-DMNs after 5000 epochs of training are listed in Table 5. It can be observed that deeper IB-DMNs slightly improve the accuracy for both training and testing data. Since the training was performed in the elastic range, the different losses are of a similar order, and, as it can be seen in Fig. 5, a similar accuracy is obtained in the linear range for the 3 different levels. Nevertheless, because of its higher flexibility the 6-level IB-DMN provides slightly more accurate results in the non-linear range, see Fig. 5. It is important to note that, compared to Table 2, reduced ranges of random material parameters, closer to real properties –such as a Poisson's ratio in the range of $(0.1, 0.45)$ and $E_{\mathrm{I}}^{\mathrm{T}}$ in the range of $(1.0, 30.0)$– were used to generate the testing data, which explains the lower error of the DMNs on the testing data.

Considering the non-linear simulations presented in Section 5, where 600 in-plane uni-axial stress and 180 in-plane shearing Direct Numerical Simulations (DNS) were conducted on the SVEs of $20\,\mu\mathrm{m} \times 20\,\mu\mathrm{m}$, it is evident that the DNS conducted on the Statistical Volume Elements (SVEs) are time-consuming, particularly for the in-plane shearing case, see Table 2. For some SVEs, one single direct shearing test could take over 100 hours. In contrast, the IB-DMNs, as surrogate models, demonstrate significant computational efficiency, completing the simulations within a few seconds. The relative efficiency of the surrogate model becomes even more pronounced when larger SVEs are used in the DNS, since the online computational time of the IB-DMN is independent on the size of the SVEs used to generate the data. However, it is worth mentioning that the computational time for the IB-DMN increases exponentially with the depth of the IB-DMN.

7. Conclusions

By reformulating the interaction based deep material network (IB-DMN), the constraint information, such as the phase volume fraction, is decoupled from the topological parameters of the micro-structure.

A reference IB-DMN can thus be trained using linear elastic data obtained from different SVE realisations of different phase volume fractions. This allows, on the one hand for the trained reference IB-DMN to handle arbitrary phase volume fractions, and on the other hand to construct a stochastic IB-DMN by introducing random perturbations to the topological parameters of this reference IB-DMN since those parameters represent the micro-structure organisation of this reference IB-DMN. This stochastic IB-DMN can then be used to conduct non-linear simulations in a finite deformation setting.

Using a unidirectional fibre-reinforced composite as an example, we demonstrate that the stochastic IB-DMN effectively captures the stochastic characteristics of the uncertain non-linear response of composite SVE realisations, if suitable parameters are used to generate the random perturbations applied to the topological parameters. This validates the feasibility or proof of concept of building a stochastic IB-DMN to act as an efficient surrogate for the stochastic homogenisation of heterogeneous materials in the non-linear range. Nevertheless, the parameters for generating random perturbations, such as α and β in Beta(α, β) and bound b, must be selected carefully, as they determine the stochastic characteristics of the non-linear response of heterogeneous materials predicted by the stochastic IB-DMN. A more rigorous determination of these parameters will be achieved in a future work, *e.g.* through a Bayesian inference.

We can however point out the following observation. During the initial training of the reference IB-DMN, a narrow range for the random initialisation of the topological parameters (*e.g.* $(-0.5, 0.5)$ as used in this work) should be employed. This helps reducing the influence of the initial values during training and prevents the final topological parameters from reaching extremely large or small values, which could increase the likelihood of obtaining parameters leading to convergence problems in the online simulation.

While the proposed stochastic DMN was applied to a two-phase material in a 2D case, its extension to multi-phase systems in 3D is straightforward.

Acknowledgment

This project has received funding from the European Union's Horizon Europe Framework Programme under grant agreement No. 101056682 for the project "DIgital DEsign strategies to certify and mAnufacture Robust cOmposite sTructures (DIDEAROT)". The contents of this publication are the sole responsibility of ULiege and do not necessarily reflect the opinion of the European Union. Neither the European Union nor the granting authority can be held responsible for them.

Data availability

The raw/processed data required to reproduce these findings is available on `https://gitlab.uliege.be/didearot/didearotPublic/publicationsData/2025_StochasticIBDMN` under the Creative Commons Attribution 4.0 International (CC BY 4.0) licence [58].

Appendix A. Non-linear IB-DMN in a finite strain setting

In the finite strain setting, we consider as a strain measure the deformation gradient $\mathbf{F} = \boldsymbol{x} \otimes \boldsymbol{\nabla}_0$, which is defined as the gradient of the deformation mapping $\boldsymbol{x}$ with respect to each component of the reference material point $\boldsymbol{X}$, with the gradient with respect to the reference configuration denoted by $\boldsymbol{\nabla}_0$. The first Piola-Kirchhoff stress tensor $\mathbf{P}$ is used as a stress measure.

Appendix A.1. Definition of the interactions

The theory reported in Section 2 can readily be formulated in a finite-strain setting, and is summarised in this appendix; we refer to [46] for more details.

Appendix A.1.1. Micro-scale interaction mechanism and homogenisation

Using the deformation gradient $\mathbf{F}$ and the first Piola-Kirchhoff stress tensor $\mathbf{P}$, the volume-averaged strain and stress relations, Eq. (1) in a small-strain setting, read in a finite strain setting as

$$\mathbf{F}_{\mathrm{M}} = \sum_{i=0}^{N_{\mathrm{p}}-1} v_i \mathbf{F}_i \,, \quad \text{and} \quad \mathbf{P}_{\mathrm{M}} = \sum_{i=0}^{N_{\mathrm{p}}-1} v_i \mathbf{P}_i \,, \tag{A.1}$$

where $\mathbf{F}_{\mathrm{M}}$ and $\mathbf{P}_{\mathrm{M}}$ are the volume-averaged deformation gradient and stress for the entire aggregation, respectively, and where $\mathbf{F}_i$ and $\mathbf{P}_i$ are the volume-averaged deformation gradient and stress in each phase Ω_i, respectively.

Appendix A.1.2. Microscopic strain

The displacement field $\boldsymbol{u}_{\mathrm{m}}(\boldsymbol{X}_{\mathrm{m}})$ in Ω_{M}, subject to a homogenised deformation gradient $\mathbf{F}_{\mathrm{M}}$, reads,

$$\boldsymbol{u}_{\mathrm{m}}(\boldsymbol{X}_{\mathrm{m}}) = (\mathbf{F}_{\mathrm{M}} - \mathbf{I}) \cdot (\boldsymbol{X}_{\mathrm{m}} - \boldsymbol{X}_{\mathrm{m}_0}) + \boldsymbol{a}(\boldsymbol{X}_{\mathrm{m}}), \quad \boldsymbol{X}_{\mathrm{m}} \in \Omega_{\mathrm{M}}, \tag{A.2}$$

where the fluctuation field $\boldsymbol{a}(\boldsymbol{X}_{\mathrm{m}})$ should satisfy

$$\sum_{i=0}^{N_{\mathrm{p}}-1} \int_{\Omega_i} \boldsymbol{a}(\boldsymbol{X}_{\mathrm{m}}) \otimes \boldsymbol{\nabla}_0 \mathrm{d}V = \mathbf{0} \,. \tag{A.3}$$

By selecting a periodic fluctuation $\boldsymbol{a}(\boldsymbol{X}_{\mathrm{m}})$ at the outer boundary, defining $\boldsymbol{a}_j = \frac{1}{s_j^i} \int_{\Gamma_{\mathrm{I}_j^i}} \boldsymbol{a}(\boldsymbol{X}_{\mathrm{m}}) \mathrm{d}s$ and the surface parameter $s_j^i = \int_{\Gamma_{\mathrm{I}_j^i}} \mathrm{d}s$ for $\Gamma_{\mathrm{I}_j^i} \neq \emptyset$, following the same developments as in Section 2.2 allow the volume-averaged deformation gradient in each phase Ω_i to be expressed in terms of the fluctuation field following

$$\mathbf{F}_i \;\; = \;\; \mathbf{F}_{\mathrm{M}} + \frac{1}{V_i} \sum_{\forall \Gamma_{\mathrm{I}_j^i} \neq \emptyset} s_j^i \boldsymbol{a}_j \otimes \boldsymbol{N}_{\mathrm{I}_j^i} \,. \tag{A.4}$$

Appendix A.1.3. Hill-Mandel condition

Following the same developments as in Section 2.3, the energy consistency between the scales, written under the form

$$\mathbf{P}_{\mathrm{M}} : \delta\mathbf{F}_{\mathrm{M}} = \sum_{i=0}^{N_{\mathrm{p}}-1} v_i \mathbf{P}_i : \delta\mathbf{F}_i \,, \tag{A.5}$$

implies the weak form

$$\sum_{i=0}^{N_{\mathrm{p}}-1} \sum_{\forall \Gamma_{\mathrm{I}_j^i} \neq \emptyset} \frac{v_i s_j^i}{V_i} \mathbf{P}_i : \left(\delta\boldsymbol{a}_j \otimes \boldsymbol{N}_{\mathrm{I}_j^i} \right) = 0 \,. \tag{A.6}$$

The constitutive model considered for phase Ω_i is stated in a finite-strain setting as

$$\mathbf{P}_i = \mathbf{P}^p \left(\mathbf{F}_i(\boldsymbol{a}_j);\, \boldsymbol{\psi}_i \right) \,, \text{ for } i = 0, \ldots, N_{\mathrm{p}} - 1,\; j = 0, 1, \ldots, N_{\mathrm{I}} - 1 \,, \tag{A.7}$$

where $\boldsymbol{\psi}_i$ is the set of internal variables.

Appendix A.1.4. Microscopic stress

In the absence of dynamics and body forces, the equilibrium equation for the aggregate, Ω_{M}, is given by

$$\mathbf{P}_{\mathrm{m}}(\boldsymbol{X}_{\mathrm{m}}) \cdot \boldsymbol{\nabla}_0 = \mathbf{0} \,, \text{ for } \boldsymbol{X}_{\mathrm{m}} \in \Omega_{\mathrm{M}} \,, \tag{A.8}$$

which, considering the averaged stress $\mathbf{P}_i$ in each subdomain Ω_i, $i = 0, \ldots, N_{\mathrm{p}} - 1$, and following the lines on Section 2.4, is approximated by

$$\sum_{i=0}^{N_{\mathrm{p}}-1} \int_{\Gamma_{\mathrm{I}_j^i}} \mathbf{P}_i \cdot \boldsymbol{N}_{\mathrm{I}_j^i} \mathrm{d}s = \sum_{i=0}^{N_{\mathrm{p}}-1} s_j^i \mathbf{P}_i \cdot \boldsymbol{N}_{\mathrm{I}_j^i} = \mathbf{0} \,, \text{ for } j = 0, \ldots, N_{\mathrm{I}} - 1 \,. \tag{A.9}$$

Appendix A.2. Resolution

When considering an IB-DMN with a binary tree structure, the equilibrium equation at the node interfaces, Eq. (32), cannot be solved directly from the strain measure, Eq. (22), in a finite-strain setting and/or when non-linear material models are considered at the material nodes, Eq. (A.7). Indeed, considering a planar surface $\Gamma_{\rm AB}$ of surface area $s_{\rm AB}$, with the outward unit normal $\boldsymbol{N}_{\rm A}$ for domain $\Omega_{\rm A}$ and $\boldsymbol{N}_{\rm B}$ for $\Omega_{\rm B}$, where $\boldsymbol{N}_{\rm B} = -\boldsymbol{N}_{\rm A}$, see Fig. 2(a), the unknown normalised fluctuation $\hat{\boldsymbol{a}} = \frac{s_{\rm AB}}{V_{\rm M}}\boldsymbol{a}$ can only be obtained from an iterative process until satisfying the interface equilibrium equations.

In the following, we consider a L-level binary tree structure. We define the vector $\mathcal{A}$ gathering the fluctuations $\hat{\mathbf{a}}$, see Eq. (21), at all the nodes N_l^k, $l < L$, where the interactions are defined. The components of this vector are ordered following their position in the binary tree: $\mathrm{pos}\left(\mathrm{N}_l^k\right) = 2^l - 1 + k$. Thus, the dimension of this vector is $3 \times (2^L - 1)$ for the 3D case, and the normalised fluctuation associated to the node N_l^k reads

$$\hat{\mathrm{a}}[d] = \mathcal{A}[3 \times \mathrm{pos}\left(\mathrm{N}_l^k\right) + d]\,, \text{ with } d = 0, 1, 2\,. \tag{A.10}$$

For the sake of conciseness, we note the fluctuation associated to node N_l^k by $\hat{\mathbf{a}}_p$, with $p = \mathrm{pos}\left(\mathrm{N}_l^k\right)$, and its topological parameters by $\mathbf{N}_{\mathrm{A}p}$ and $v_{\mathrm{A}p}$. The topological parameters are directly available from the topological parameter lists evaluated at location p, *i.e.*, following the notations of Section 4, as $\mathcal{T}_{\rm n}[p]$ and $\mathcal{T}_{\rm v}[p]$, using Eqs. (34), (35) and either (38) or (39) for $l = L - 1$.

Appendix A.2.1. The local deformation gradient at nodes N_l^k, $l < L$

The deformation gradient tensor is expressed in a vector form following

$$\mathcal{F} = [F_{00},\, F_{01},\, F_{02},\, F_{10},\, \ldots,\, F_{21},\, F_{22}]^{\mathrm{T}}\,. \tag{A.11}$$

We rewrite the Eq. (31) in a matrix operations form and in a finite-strain setting as

$$\mathcal{F}_{\rm A} = \mathcal{F}_{\rm M} + \frac{1}{v_{\rm A}}\mathbf{N}_{\rm A}\hat{\mathbf{a}}\,, \text{ and } \mathcal{F}_{\rm B} = \mathcal{F}_{\rm M} - \frac{1}{1.0 - v_{\rm A}}\mathbf{N}_{\rm A}\hat{\mathbf{a}}\,, \tag{A.12}$$

where

$$\mathbf{N}_{\rm A} = \begin{bmatrix} N_0 & N_1 & N_2 & 0 & 0 & 0 & 0 & 0 & 0 \\ 0 & 0 & 0 & N_0 & N_1 & N_2 & 0 & 0 & 0 \\ 0 & 0 & 0 & 0 & 0 & 0 & N_0 & N_1 & N_2 \end{bmatrix}^{\mathrm{T}}_{\mathrm{A}}\,, \tag{A.13}$$

For a given macroscopic deformation gradient $\mathbf{F}_{\rm M}$, the local deformation gradient, at each node N_l^k, $l = 0, ..., L$, can be computed through the following process,

- $\mathbf{F}(\mathrm{N}_0^0) = \mathbf{F}_{\rm M}\,.$
- If the deformation gradient $\mathbf{F}\left(\mathrm{N}_l^k\right)$ at a node N_l^k and the fluctuation $\hat{\mathbf{a}}_p$, with $p = \mathrm{pos}(\mathrm{N}_l^k)$, at the interaction interface associated to the node N_l^k are known, then for its two direct children nodes, N_{l+1}^{2k} and N_{l+1}^{2k+1}, we have in the matrix form

$$\mathcal{F}(\mathrm{N}_{l+1}^{2k+r}) = \mathcal{F}\left(\mathrm{N}_l^k\right) + (1-r)\frac{1}{v_{\mathrm{A}p}}\mathbf{N}_{\mathrm{A}p}\hat{\mathbf{a}}_p - r\frac{1}{1.0 - v_{\mathrm{A}p}}\mathbf{N}_{\mathrm{A}p}\hat{\mathbf{a}}_p \text{ with } r = 0,\, 1\,. \tag{A.14}$$

Appendix A.2.2. The deformation gradient at the material nodes N_L^k

According to Eq. (A.14), the deformation gradient at a given material node N_L^k at the level "L" can be evaluated by the topological parameters and the associated fluctuations of all its parent nodes. Using the fluctuation vector $\mathcal{A}$, this deformation gradient expressed in the vector form reads,

$$\mathcal{F}(\mathrm{N}_L^k) = \mathcal{F}(\mathrm{N}_0^0) + \left[\underline{\mathbf{n}}_0^k\,, ...\,, \mathbf{0}\,, \underbrace{\underline{\mathbf{n}}_l^k}_{\mathrm{pos}(\mathrm{N}_l^{q_l})}\,, \mathbf{0}\,, ...\right]\mathcal{A}\,,\ \text{with } l = 1, ..., L-1\,, \tag{A.15}$$

where $\mathrm{N}_l^{q_l}$ is the parent node of N_L^k at level l, and where $\underline{\mathbf{n}}_l^k$ is a 9×3 matrix for the 3D case, which reads

$$\underline{\mathbf{n}}_l^k = (1 - r_l)\frac{1}{v_{\mathrm{A}p}}\mathbf{N}_{\mathrm{A}p} - r_l\frac{1}{1.0 - v_{\mathrm{A}p}}\mathbf{N}_{\mathrm{A}p}\,,\ \text{with } p = \mathrm{pos}(\mathrm{N}_l^{q_l})\,. \tag{A.16}$$

For a material node at level "L", its parent nodes can be traced as follows

$$\begin{aligned}
\mathrm{N}_L^k &\rightarrow \mathrm{N}_{L-1}^{q_{L-1}},\ \text{with } q_{L-1} = k//2\,, r_{L-1} = k\%2\,,\\
\mathrm{N}_{L-1}^{q_{L-1}} &\rightarrow \mathrm{N}_{L-2}^{q_{L-2}},\ \text{with } q_{L-2} = q_{L-1}//2\,, r_{L-2} = q_{L-1}\%2\,,\\
&... \qquad ...\\
\mathrm{N}_1^{q_1} &\rightarrow \mathrm{N}_0^{q_0},\ \text{with } r_0 = q_1\%2\,,
\end{aligned} \tag{A.17}$$

where $k = 0$, 1, ..., $2^L - 1$, and where // and % represent the operations to compute respectively the quotient and remainder.

Using the expression of Eq. (A.15), we can gather the deformation gradients at all the material nodes at level L in the vector $\mathcal{E}$, of length 9×2^L for the 3D case, with

$$\mathcal{E} = \mathcal{I}\mathcal{F}_{\mathrm{M}} + \mathcal{N}_{\mathrm{v}}\mathcal{A}\,,\ \text{with } \mathcal{N}_{\mathrm{v}} = \begin{bmatrix} \underline{\mathbf{n}}_0^0 & \cdots & \underline{\mathbf{n}}_l^0 & \cdots \\ \underline{\mathbf{n}}_0^1 & \cdots & \underline{\mathbf{n}}_l^1 & \cdots \\ \cdots & \cdots & \cdots & \cdots \\ \underline{\mathbf{n}}_0^{2^L-1} & \cdots & \underline{\mathbf{n}}_l^{2^L-1} & \cdots \end{bmatrix}, \tag{A.18}$$

where $\mathcal{I} = [\underbrace{\mathbf{I}, \mathbf{I}, ..., \mathbf{I}}_{2^L \text{ repeat}}]^{\mathrm{T}}$, and where $\mathbf{I}$ is a 9×9 identity matrix.

Appendix A.2.3. The stress tensors at the material nodes

Knowing the deformation gradient of each material node at level L, the stresses at these material nodes, $\mathbf{P}(\mathrm{N}_L^k)$, can be evaluated using their respective constitutive laws. The stress tensors $\mathbf{P}(\mathrm{N}_l^q)$ at the other nodes are computed following

$$\mathbf{P}(\mathrm{N}_l^q) = v_{\mathrm{A}p}\mathbf{P}(\mathrm{N}_{l+1}^{2q}) + (1.0 - v_{\mathrm{A}p})\mathbf{P}(\mathrm{N}_{l+1}^{2q+1})\,,\ \text{with } p = \mathrm{pos}(\mathrm{N}_l^q)\,, \tag{A.19}$$

where $l = L - 1$, ..., 1, 0.

The stress tensors $\mathbf{P}(\mathrm{N}_L^q)$ at the material nodes of level "L" written under the vector form $\mathcal{P}(\mathrm{N}_L^q)$ with the same convention as for the deformation gradient, Eq. (A.11), are gathered under a global stress vector $\mathcal{S}$, of length 9×2^L for the 3D case. The stress tensors at material nodes at level "L" can then be extracted from the matrix operation following

$$\mathcal{P}(\mathrm{N}_L^k) = \left[... \quad \mathbf{0} \quad \underbrace{\mathbf{I}}_{k} \quad \mathbf{0} \quad ...\right]\mathcal{S}\,. \tag{A.20}$$

Using Eq. (A.19), the stress tensors at level "$L - 1$" can be extracted following

$$\mathcal{P}(\mathrm{N}_{L-1}^q) \;=\; \left[... \quad \mathbf{0} \quad v_{\mathrm{A}p}\mathbf{I} \quad (1.0 - v_{\mathrm{A}p})\mathbf{I} \quad \mathbf{0} \quad ...\right]\mathcal{S}\,, \tag{A.21}$$

where $p = \text{pos}(\text{N}_{L-1}^q)$.

Using Eq. (A.19), the stress at nodes at levels "$l < L-1$" can then be recursively obtained from the stress tensors vector $\mathcal{S}$ and the topological parameters $\underline{\mathcal{T}}_\text{v}$. As a result, using Eqs. (A.19)-(A.21), the stress tensor at any node at levels $0 < l \leq L$ can be computed by a unified formula, $\mathcal{V}\mathcal{S}$, where $\mathcal{V}$ keeps the information of the volume fraction v_A at the different interaction nodes of level "$0 < l < L$" and the identity matrix at level $l = L$, in which we did not consider the first row corresponding to node N_0^0 when constructing the matrix $\mathcal{V}$.

Appendix A.2.4. Equilibrium at the interface nodes at level "$l < L$"

The equilibrium equation (A.9) at the interface of material node N_l^q, $l = 0, ..., L-1$, reads in its matrix form

$$\mathbf{N}_{\text{A}p}^\text{T}\left[\mathcal{P}(\text{N}_{l+1}^{2q}) - \mathcal{P}(\text{N}_{l+1}^{2q+1})\right] = \mathbf{0}\,, \tag{A.22}$$

$$\mathbf{N}_{\text{A}p}^\text{T}\left[\mathcal{V}(\text{N}_{l+1}^{2q}) - \mathcal{V}(\text{N}_{l+1}^{2q+1})\right]\mathcal{S} = \mathbf{0}\,, \tag{A.23}$$

where $p = \text{pos}(\text{N}_l^q)$, $\mathcal{V}(\text{N}_{l+1}^{2q})$ and $\mathcal{V}(\text{N}_{l+1}^{2q+1})$ are the two rows of the matrix $\mathcal{V}$ corresponding to the the nodes N_{l+1}^{2q} and N_{l+1}^{2q+1}, respectively.

Excluding the row corresponding to the node N_0^0 in the matrix $\mathcal{V}$, the equilibrium equations (A.23) can be rewritten for all the nodes with an interface interaction as

$$\mathcal{N}_\text{T}\mathcal{V}\mathcal{S} = \mathbf{0}\,, \tag{A.24}$$

where the matrix $\mathcal{N}_\text{T}$ combines all the matrices $\mathbf{N}_{\text{A}p}^\text{T}$ of dimension 3×9 associated to the interaction nodes.

Appendix A.2.5. Iterative resolution of the non-linear equations

Using the topological parameters $\underline{\mathcal{T}}_\text{n}$ and $\underline{\mathcal{T}}_\text{v}$ defined in Section 4, the matrices $\mathcal{N}_v$, $\mathcal{V}$ and $\mathcal{N}_\text{T}$ are constructed following Eqs. (A.13), (A.16), (A.18) and (A.23) at the beginning of the online stage and remain constant throughout the simulations. The equilibrium Eq. (A.24) is solved iteratively using a Newton-Raphson method as follows

- Initialisation: The macroscopic deformation gradient $\mathbf{F}_\text{M}$ is known. The fluctuation vector is first initialised as $\mathcal{A} = \mathcal{A}_0$, with *e.g.* $\mathcal{A}_0 = \mathbf{0}$.
- Step 1: Submitting $\mathbf{F}_\text{M}$ and $\mathcal{A}$ into Eq. (A.18), allows computing the deformation gradients $\mathcal{E}$ at the material nodes at level "L". The stress vector $\mathcal{S}$ is evaluated using the constitutive models (A.19).
- Step 2: The residual vector $\mathcal{R}$ of the equilibrium equations (A.24) is evaluated as

  $$\mathcal{R} = \mathcal{N}_\text{T}\mathcal{V}\mathcal{S}\,, \tag{A.25}$$

  and is submitted to a convergence criterion $\|\mathcal{R}\| <$ Tolerance.
  If the criterion is satisfied, iterations are stopped.
  If not, we proceed to Step 3.
- Step 3: Under the condition of constant $\mathbf{F}_\text{M}$, the derivative of $\mathcal{R}$ with respect to $\mathcal{A}$ is computed through the differentiation chain rule

  $$\text{d}\mathcal{R} = \mathcal{N}_\text{T}\mathcal{V}\text{d}\mathcal{S}\,, \tag{A.26}$$

  $$\text{d}\mathcal{R} = \mathcal{N}_\text{T}\mathcal{V}\frac{\text{d}\mathcal{S}}{\text{d}\mathcal{E}}\frac{\partial\mathcal{E}}{\partial\mathcal{A}}\text{d}\mathcal{A}\,, \tag{A.27}$$

  $$\frac{\text{d}\mathcal{R}}{\text{d}\mathcal{A}} = \mathcal{N}_\text{T}\mathcal{V}\mathcal{C}\mathcal{N}_\text{v}\,, \tag{A.28}$$

  where the matrix $\mathcal{C}$ is an assembly of the tangent operators $\frac{\text{d}\mathbf{P}}{\text{d}\mathbf{F}}$, written under a matrix form, of the material nodes at level "L".

- Step 4: The fluctuation vector is updated following

$$\mathcal{A} \leftarrow \mathcal{A} - \left(\frac{\mathrm{d}\mathcal{R}}{\mathrm{d}\mathcal{A}}\right)^{-1} \mathcal{R}\,, \tag{A.29}$$

  to proceed to a new iteration at Step 1.

Appendix A.3. Up-scaling for macroscopic simulations

After solving Eq. (A.24), we have the homogenised stress, which reads

$$\mathcal{P}_{\mathrm{M}} = \mathcal{P}(\mathrm{N}_0^0) = \left[v_{\mathrm{A}0}\mathcal{V}\left(\mathrm{N}_1^0\right) + (1.0 - v_{\mathrm{A}0})\mathcal{V}\left(\mathrm{N}_1^1\right)\right]\mathcal{S}\,. \tag{A.30}$$

In order to extract the homogenised algorithmic tensor, the equilibrium equation (A.25) ought to be satisfied for a perturbation of the macro-scale quantities, *i.e.*

$$\mathrm{d}\mathcal{R} \;=\; \mathcal{N}_{\mathrm{T}}\mathcal{V}\mathrm{d}\mathcal{S} = \mathbf{0}\,. \tag{A.31}$$

Then, considering a variation of the homogenised deformation gradient yields

$$\mathcal{N}_{\mathrm{T}}\mathcal{V}\frac{\mathrm{d}\mathcal{S}}{\mathrm{d}\mathcal{E}}\mathrm{d}\mathcal{E} \;=\; \mathbf{0}\,,\ \text{or} \tag{A.32}$$

$$\mathcal{N}_{\mathrm{T}}\mathcal{V}\mathcal{C}\left(\frac{\partial\mathcal{E}}{\partial\mathcal{A}}\mathrm{d}\mathcal{A} + \frac{\partial\mathcal{E}}{\partial\mathcal{F}_{\mathrm{M}}}\mathrm{d}\mathcal{F}_{\mathrm{M}}\right) \;=\; \mathbf{0}\,. \tag{A.33}$$

Using Eq. (A.18) and the expression of the homogenised stress, Eq. (A.30), the homogenised algorithmic operator reads in the matrix form

$$\frac{\mathrm{d}\mathcal{P}_{\mathrm{M}}}{\mathrm{d}\mathcal{F}_{\mathrm{M}}} \;=\; \left[v_{\mathrm{A}0}\mathcal{V}\left(\mathrm{N}_1^0\right) + (1.0 - v_{\mathrm{A}0})\,\mathcal{V}(\mathrm{N}_1^1)\right]\mathcal{C}\left[\frac{\partial\mathcal{E}}{\partial\mathcal{A}}\frac{\partial\mathcal{A}}{\partial\mathcal{F}_{\mathrm{M}}} + \frac{\partial\mathcal{E}}{\partial\mathcal{F}_{\mathrm{M}}}\right],\ \text{or} \tag{A.34}$$

$$\;=\; \left[v_{\mathrm{A}0}\mathcal{V}\left(\mathrm{N}_1^0\right) + (1.0 - v_{\mathrm{A}0})\mathcal{V}\left(\mathrm{N}_1^1\right)\right]\mathcal{C}\left[\mathcal{N}_{\mathrm{v}}\frac{\partial\mathcal{A}}{\partial\mathcal{F}_{\mathrm{M}}} + \mathcal{I}\right], \tag{A.35}$$

where $\frac{\partial\mathcal{A}}{\partial\mathcal{F}_{\mathrm{M}}} = -\left(\mathcal{N}_{\mathrm{T}}\mathcal{V}\mathcal{C}\frac{\partial\mathcal{E}}{\partial\mathcal{A}}\right)^{-1}\mathcal{N}_{\mathrm{T}}\mathcal{V}\mathcal{C}\frac{\partial\mathcal{E}}{\partial\mathcal{F}_{\mathrm{M}}} = -\left(\mathcal{N}_{\mathrm{T}}\mathcal{V}\mathcal{C}\mathcal{N}_{\mathrm{v}}\right)^{-1}\mathcal{N}_{\mathrm{T}}\mathcal{V}\mathcal{C}$ according to Eqs. (A.18) and (A.33).

Appendix B. J_2 elasto-plastic constitutive model

The matrix obeys a finite-strain J_2 elasto-plastic constitutive model [56]. The deformation gradient $\mathbf{F}$ is decomposed into the reversible elastic part $\mathbf{F}^{\mathrm{e}}$ and the irreversible plastic part $\mathbf{F}^{\mathrm{p}}$ such that $\mathbf{F} = \mathbf{F}^{\mathrm{e}} \cdot \mathbf{F}^{\mathrm{p}}$. The elastic potential energy is defined as

$$\psi_0(\mathbf{C}^{\mathrm{e}}) = \frac{K_0}{2}\ln^2 J + \frac{G_0}{4}\left(\ln\mathbf{C}^{\mathrm{e}}\right)^{\mathrm{dev}} : \left(\ln\mathbf{C}^{\mathrm{e}}\right)^{\mathrm{dev}}\,, \tag{B.1}$$

where $\mathbf{C}^{\mathrm{e}} = \mathbf{F}^{\mathrm{eT}} \cdot \mathbf{F}^{\mathrm{e}}$, and K_0 and G_0 correspond to the bulk and shear, respectively, moduli of the matrix material. The first Piola-Kirchhoff stress tensor $\mathbf{P}$ derives from the elastic potential (B.1) following

$$\mathbf{P} = \frac{\partial\psi_0\left(\mathbf{F};\mathbf{F}^{\mathrm{p}}\right)}{\partial\mathbf{F}} = K_0\mathbf{F}^{-\mathrm{T}}\ln J + G_0\mathbf{F}^{\mathrm{e}} \cdot \left[\mathbf{C}^{\mathrm{e}\,-1} \cdot \left(\ln\mathbf{C}^{\mathrm{e}}\right)^{\mathrm{dev}}\right] \cdot \mathbf{F}^{\mathrm{p}\,-\mathrm{T}}\,. \tag{B.2}$$

The elastic part $\mathbf{F}^{\mathrm{e}}$ and the plastic part $\mathbf{F}^{\mathrm{p}}$ of the deformation gradient are obtained through a J_2 plastic flow expressed in terms of the Kirchhoff stress. The Kirchhoff stress $\boldsymbol{\kappa} = \mathbf{P} \cdot \mathbf{F}^{\mathrm{T}}$ is first computed by Eq. (B.2) as

$$\boldsymbol{\kappa} = K_0\ln J\mathbf{I} + G_0\mathbf{F}^{\mathrm{e}} \cdot \left[\mathbf{C}^{\mathrm{e}-1} \cdot \left(\ln\mathbf{C}^{\mathrm{e}}\right)^{\mathrm{dev}}\right] \cdot \mathbf{F}^{\mathrm{e}\,\mathrm{T}}\,. \tag{B.3}$$

The equivalent von Mises stress is then calculated through the deviatoric part of $\boldsymbol{\kappa}$, *i.e.* $\tau_{eq} = \sqrt{\frac{3}{2}\boldsymbol{\kappa}^{\mathrm{dev}} : \boldsymbol{\kappa}^{\mathrm{dev}}}$. According to the J_2-plasticity theory, the von Mises stress criterion reads

$$f = \tau_{\mathrm{eq}} - \tau_{\mathrm{y}}^0 - R(\gamma) \leq 0\,, \tag{B.4}$$

where f is the yield surface, τ_{y}^0 is the initial yield stress, γ is the equivalent plastic strain and $R(\gamma)$ is the isotropic hardening. The evolution of $\mathbf{F}^{\mathrm{p}}$ is determined by the normal plastic flow theory following

$$\dot{\mathbf{F}}^{\mathrm{p}} = \dot{\gamma}\mathbf{N} \cdot \mathbf{F}^{\mathrm{p}}\,, \tag{B.5}$$

where $\mathbf{N}$ is the normal to the yield surface, see [56] for more details.

Appendix C. Sensitivity study on the IB-DMN training

Appendix C.1. DNS vs. *IB-DMN predictions for different sizes of the training data set*

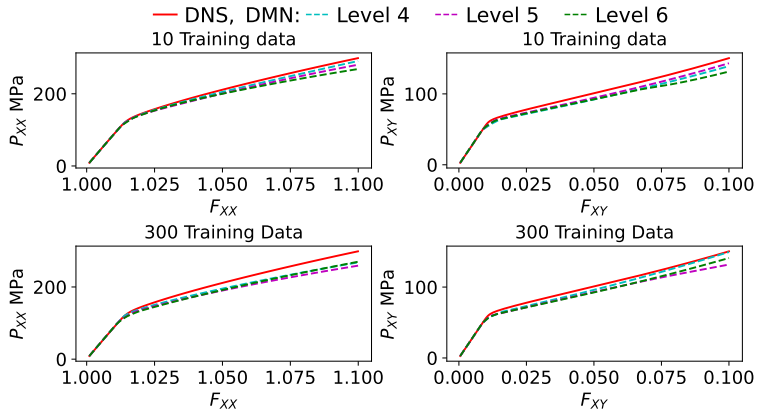

Figure C.17: The non-linear predictions of the 4-, 5- and 6-level IB-DMNs for the non-statistically representative volume element number 6 subjected to in-plane uni-axial stress and in-plane shearing loading conditions with different sizes of the training data set. The reference results are obtained from Direct Numerical Simulations (DNSs).

The effect of the size of the training data set is studied in Fig. C.17, where is can be seen that increasing the number of training data from 10 to 300 does not improve the predictions for all the loading cases.

Appendix C.2. DNS vs. *IB-DMN predictions in an infinitesimal setting*

The fibres are assumed to be isotropic linear elastic with Young's modulus $E_{\mathrm{I}} = 32$ GPa and Poisson's ratio $\nu_{\mathrm{I}} = 0.2$. The matrix obeys a J_2 elasto-plastic constitutive model with a linear isotropic hardening, and its material constants are a Young's modulus $E_0 = 3.2$ GPa, a Poisson ratio $\nu_0 = 0.3$, an initial yield stress $\sigma_{\mathrm{y}}^0 = 100$ MPa and a hardening modulus $h_0 = 6.4$ MPa. The six non-statistically representative volume elements of different volume fractions are subjected to the in-plane uni-axial stress loading condition. The prediction of the IB-DMNs in an infinitesimal setting are plotted in Fig. C.18 together with the reference results obtained from the direct numerical simulations, also obtained in an infinitesimal setting.

References

[1] M. Ostoja-Starzewski, S. Kale, P. Karimi, A. Malyarenko, B. Raghavan, S. Ranganathan, J. Zhang, Chapter two - scaling to rve in random media, volume 49 of *Advances in Applied Mechanics*, Elsevier, 2016, pp. 111–211. URL: `https://www.sciencedirect.com/science/article/pii/S0065215616300011`. doi:`https://doi.org/10.1016/bs.aams.2016.07.001`.

[2] L. Noels, Chapter one - toward stochastic multiscale methods in continuum solid mechanics, volume 55 of *Advances in Applied Mechanics*, Elsevier, 2022, pp. 1–254. URL: `https://www.sciencedirect.com/science/article/pii/S0065215622000011`. doi:`https://doi.org/10.1016/bs.aams.2022.03.001`.

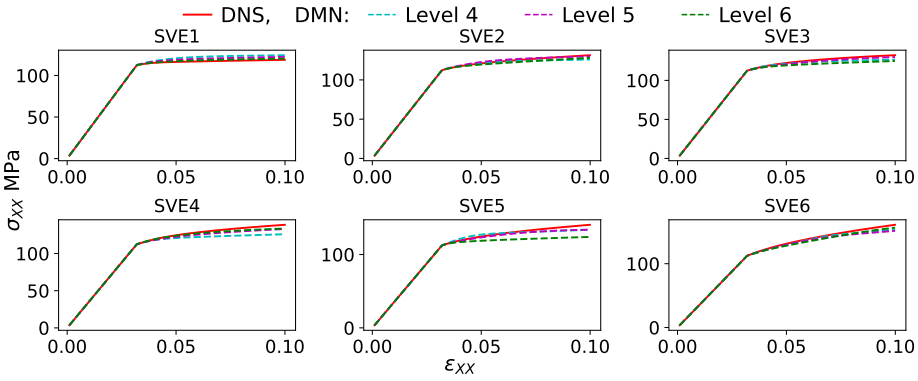

Figure C.18: The non-linear predictions in an infinitesimal setting of the 4-, 5- and 6-level IB-DMNs for the six non-statistically representative volume elements of different volume fractions subjected to an in-plane uni-axial stress loading condition. The reference results are obtained from Direct Numerical Simulations (DNSs) in an infinitesimal setting.

[3] M. Ostoja-Starzewski, X. Du, Z. F. Khisaeva, W. Li, Comparisons of the size of the representative volume element in elastic, plastic, thermoelastic, and permeable random microstructures, International Journal for Multiscale Computational Engineering 5 (2007) 73–82.

[4] M. Salmi, F. Auslender, M. Bornert, M. Fogli, Apparent and effective mechanical properties of linear matrix-inclusion random composites: Improved bounds for the effective behavior, International Journal of Solids and Structures 49 (2012) 1195 – 1211. doi:10.1016/j.ijsolstr.2012.01.018.

[5] P. Trovalusci, M. L. De Bellis, M. Ostoja-Starzewski, A. Murrali, Particulate random composites homogenized as micropolar materials, Meccanica 49 (2014) 2719–2727. doi:10.1007/s11012-014-0031-x.

[6] P. Trovalusci, M. Ostoja-Starzewski, M. L. De Bellis, A. Murrali, Scale-dependent homogenization of random composites as micropolar continua, European Journal of Mechanics - A/Solids 49 (2015) 396 – 407. doi:10.1016/j.euromechsol.2014.08.010.

[7] E. Reccia, M. L. De Bellis, P. Trovalusci, R. Masiani, Sensitivity to material contrast in homogenization of random particle composites as micropolar continua, Composites Part B: Engineering 136 (2018) 39 – 45. doi:10.1016/j.compositesb.2017.10.017.

[8] T. Kanit, S. Forest, I. Galliet, V. Mounoury, D. Jeulin, Determination of the size of the representative volume element for random composites: statistical and numerical approach, International Journal of Solids and Structures 40 (2003) 3647 – 3679. doi:10.1016/S0020-7683(03)00143-4.

[9] S. Mariani, R. Martini, A. Ghisi, A. Corigliano, M. Beghi, Overall elastic properties of polysilicon films: a statistical investigation of the effects of polycrystal morphology, International Journal for Multiscale Computational Engineering 9 (2011) 327–346.

[10] M. Geißendörfer, A. Liebscher, C. Proppe, C. Redenbach, D. Schwarzer, Stochastic multiscale modeling of metal foams, Probabilistic Engineering Mechanics 37 (2014) 132 – 137. doi:10.1016/j.probengmech.2014.06.006.

[11] V. Lucas, J.-C. Golinval, S. Paquay, V.-D. Nguyen, L. Noels, L. Wu, A stochastic computational multiscale approach; application to mems resonators, Computer Methods in Applied Mechanics and Engineering 294 (2015) 141–167. URL: https://www.sciencedirect.com/science/article/pii/S0045782515001929. doi:https://doi.org/10.1016/j.cma.2015.05.019.

[12] G. Stefanou, D. Savvas, M. Papadrakakis, Stochastic finite element analysis of composite structures based on material microstructure, Composite Structures 132 (2015) 384 – 392. doi:10.1016/j.compstruct.2015.05.044.

[13] D. Savvas, G. Stefanou, M. Papadrakakis, Determination of rve size for random composites with local volume fraction variation, Computer Methods in Applied Mechanics and Engineering 305 (2016) 340 – 358. doi:10.1016/j.cma.2016.03.002.

[14] G. Stefanou, D. Savvas, M. Papadrakakis, Stochastic finite element analysis of composite structures based on mesoscale random fields of material properties, Computer Methods in Applied Mechanics and Engineering 326 (2017) 319 – 337. doi:10.1016/j.cma.2017.08.002.

[15] L. Wu, C. N. Chung, Z. Major, L. Adam, L. Noels, From SEM images to elastic responses: A stochastic multiscale analysis of UD fiber reinforced composites, Composite Structures 189 (2018) 206 – 227. doi:10.1016/j.compstruct.2018.01.051.

[16] L. Wu, V. Lucas, V.-D. Nguyen, J.-C. Golinval, S. Paquay, L. Noels, A stochastic multi-scale approach for the modeling of thermo-elastic damping in micro-resonators, Computer Methods in Applied Mechanics and Engineering 310 (2016) 802 – 839. URL: http://www.sciencedirect.com/science/article/pii/S0045782516303930. doi:http://dx.doi.org/10.1016/j.cma.2016.07.042.

[17] V. Lucas, J.-C. Golinval, R. C. Voicu, M. Danila, R. Gavrila, R. Müller, A. Dinescu, L. Noels, L. Wu, Propagation of material and surface profile uncertainties on mems micro-resonators using a stochastic second-order computational multiscale approach, International Journal for Numerical Methods in Engineering 111 (2017) 26–68. doi:10.1002/nme.5452.

[18] D.-A. Hun, J. Guilleminot, J. Yvonnet, M. Bornert, Stochastic multiscale modeling of crack propagation in random heterogeneous media, International Journal for Numerical Methods in Engineering 119 (2019) 1325–1344. doi:10.1002/

nme.6093.
[19] C. Soize, Random matrix theory for modeling uncertainties in computational mechanics, Computer Methods in Applied Mechanics and Engineering 194 (2005) 1333 – 1366. doi:10.1016/j.cma.2004.06.038, special Issue on Computational Methods in Stochastic Mechanics and Reliability Analysis.
[20] C. Soize, Non-gaussian positive-definite matrix-valued random fields for elliptic stochastic partial differential operators, Computer Methods in Applied Mechanics and Engineering 195 (2006) 26 – 64. doi:10.1016/j.cma.2004.12.014.
[21] J. Guilleminot, A. Noshadravan, C. Soize, R. G. Ghanem, A probabilistic model for bounded elasticity tensor random fields with application to polycrystalline microstructures, Computer Methods in Applied Mechanics and Engineering 200 (2011) 1637 – 1648. doi:10.1016/j.cma.2011.01.016.
[22] A. Noshadravan, R. Ghanem, J. Guilleminot, I. Atodaria, P. Peralta, Validation of a probabilistic model for mesoscale elasticity tensor or random polycrystals, International Journal for Uncertainty Quantification 3 (2013) 73–100. doi:10.1615/Int.J.UncertaintyQuantification.2012003901.
[23] A. Malyarenko, M. Ostoja-Starzewski, Spectral expansions of homogeneous and isotropic tensor-valued random fields, Zeitschrift für angewandte Mathematik und Physik 59 (2016) 59. doi:10.1007/s00033-016-0657-8.
[24] A. Malyarenko, M. Ostoja-Starzewski, Tensor-valued random fields in continuum physics, in: P. Trovalusci (Ed.), Materials with Internal Structure: Multiscale and Multifield Modeling and Simulation, Springer International Publishing, Cham, 2016, pp. 75–87. doi:10.1007/978-3-319-21494-8_6.
[25] A. Malyarenko, M. Ostoja-Starzewski, A random field formulation of hooke's law in all elasticity classes, Journal of Elasticity 127 (2017) 269–302. doi:10.1007/s10659-016-9613-2.
[26] M. Tootkaboni, L. Graham-Brady, A multi-scale spectral stochastic method for homogenization of multi-phase periodic composites with random material properties, International Journal for Numerical Methods in Engineering 83 (2010) 59–90. doi:10.1002/nme.2829.
[27] X. Xu, L. Graham-Brady, A stochastic computational method for evaluation of global and local behavior of random elastic media, Computer Methods in Applied Mechanics and Engineering 194 (2005) 4362 – 4385. doi:10.1016/j.cma.2004.12.001.
[28] D. Pivovarov, P. Steinmann, Modified sfem for computational homogenization of heterogeneous materials with microstructural geometric uncertainties, Computational Mechanics 57 (2016) 123–147.
[29] D. Pivovarov, P. Steinmann, K. Willner, Two reduction methods for stochastic fem based homogenization using global basis functions, Computer Methods in Applied Mechanics and Engineering 332 (2018) 488 – 519. doi:10.1016/j.cma.2018.01.002.
[30] M. G. D. Geers, V. G. Kouznetsova, W. A. M. Brekelmans, Multi-scale computational homogenization: Trends and challenges, Journal of Computational and Applied Mathematics 234 (2010) 2175–2182. doi:DOI:10.1016/j.cam.2009.08.077, fourth International Conference on Advanced COmputational Methods in ENgineering (ACOMEN 2008).
[31] L. Noels, L. Wu, L. Adam, J. Seyfarth, G. Soni, J. Segurado, G. Laschet, G. Chen, M. Lesueur, M. Lobos, T. Böhlke, T. Reiter, S. Oberpeilsteiner, D. Salaberger, D. Weichert, C. Broeckmann, Effective Properties, John Wiley & Sons, Ltd, 2016, pp. 433–485. URL: https://onlinelibrary.wiley.com/doi/abs/10.1002/9783527693566.ch6. doi:10.1002/9783527693566.ch6. arXiv:https://onlinelibrary.wiley.com/doi/pdf/10.1002/9783527693566.ch6.
[32] J. Yvonnet, Q.-C. He, The reduced model multiscale method (r3m) for the non-linear homogenization of hyperelastic media at finite strains, Journal of Computational Physics 223 (2007) 341–368. URL: https://www.sciencedirect.com/science/article/pii/S0021999106004402. doi:https://doi.org/10.1016/j.jcp.2006.09.019.
[33] Z. Liu, M. Bessa, W. K. Liu, Self-consistent clustering analysis: An efficient multi-scale scheme for inelastic heterogeneous materials, Computer Methods in Applied Mechanics and Engineering 306 (2016) 319–341. URL: https://www.sciencedirect.com/science/article/pii/S0045782516301499. doi:https://doi.org/10.1016/j.cma.2016.04.004.
[34] T. Huang, J. Gao, Q. Sun, D. Zeng, X. Su, W. Kam Liu, W. Chen, Stochastic nonlinear analysis of unidirectional fiber composites using image-based microstructural uncertainty quantification, Composite Structures 260 (2021) 113470. URL: https://www.sciencedirect.com/science/article/pii/S0263822320333997. doi:https://doi.org/10.1016/j.compstruct.2020.113470.
[35] L. Wu, V.-D. Nguyen, L. Adam, L. Noels, An inverse micro-mechanical analysis toward the stochastic homogenization of nonlinear random composites, Computer Methods in Applied Mechanics and Engineering 348 (2019) 97–138. URL: https://www.sciencedirect.com/science/article/pii/S0045782519300210. doi:https://doi.org/10.1016/j.cma.2019.01.016.
[36] J. M. Calleja Vázquez, L. Wu, V.-D. Nguyen, L. Noels, A micromechanical mean-field homogenization surrogate for the stochastic multiscale analysis of composite materials failure, International Journal for Numerical Methods in Engineering 124 (2023) 5200–5262. URL: https://onlinelibrary.wiley.com/doi/abs/10.1002/nme.7344. doi:https://doi.org/10.1002/nme.7344. arXiv:https://onlinelibrary.wiley.com/doi/pdf/10.1002/nme.7344.
[37] F. Ghavamian, A. Simone, Accelerating multiscale finite element simulations of history-dependent materials using a recurrent neural network, Computer Methods in Applied Mechanics and Engineering 357 (2019) 112594. URL: http://www.sciencedirect.com/science/article/pii/S0045782519304700. doi:https://doi.org/10.1016/j.cma.2019.112594.
[38] L. Wu, V. D. Nguyen, N. G. Kilingar, L. Noels, A recurrent neural network-accelerated multi-scale model for elasto-plastic heterogeneous materials subjected to random cyclic and non-proportional loading paths, Computer Methods in Applied Mechanics and Engineering 369 (2020) 113234. URL: https://www.sciencedirect.com/science/article/pii/S0045782520304199. doi:https://doi.org/10.1016/j.cma.2020.113234.
[39] L. Wu, L. Noels, Self-consistency reinforced minimal gated recurrent unit for surrogate modeling of history-dependent nonlinear problems: Application to history-dependent homogenized response of heterogeneous materials, Computer Methods in Applied Mechanics and Engineering 424 (2024) 116881. URL: https://www.sciencedirect.com/science/article/pii/

S0045782524001373. doi:https://doi.org/10.1016/j.cma.2024.116881.
[40] X. Lu, J. Yvonnet, L. Papadopoulos, I. Kalogeris, V. Papadopoulos, A stochastic fe2 data-driven method for nonlinear multiscale modeling, Materials 14 (2021). URL: https://www.mdpi.com/1996-1944/14/11/2875. doi:10.3390/ma14112875.
[41] Z. Liu, C. Wu, M. Koishi, A deep material network for multiscale topology learning and accelerated nonlinear modeling of heterogeneous materials, Computer Methods in Applied Mechanics and Engineering 345 (2019) 1138–1168. URL: https://www.sciencedirect.com/science/article/pii/S0045782518304729. doi:https://doi.org/10.1016/j.cma.2018.09.020.
[42] Z. Liu, C. Wu, Exploring the 3d architectures of deep material network in data-driven multiscale mechanics, Journal of the Mechanics and Physics of Solids 127 (2019) 20 – 46. URL: http://www.sciencedirect.com/science/article/pii/S0022509618310688. doi:https://doi.org/10.1016/j.jmps.2019.03.004.
[43] S. Gajek, M. Schneider, T. Böhlke, On the micromechanics of deep material networks, Journal of the Mechanics and Physics of Solids 142 (2020) 103984. doi:10.1016/j.jmps.2020.103984.
[44] S. Gajek, M. Schneider, T. Böhlke, An fe–dmn method for the multiscale analysis of short fiber reinforced plastic components, Computer Methods in Applied Mechanics and Engineering 384 (2021) 113952. URL: https://www.sciencedirect.com/science/article/pii/S0045782521002899. doi:https://doi.org/10.1016/j.cma.2021.113952.
[45] Z. Liu, Cell division in deep material networks applied to multiscale strain localization modeling, Computer Methods in Applied Mechanics and Engineering 384 (2021) 113914. URL: https://www.sciencedirect.com/science/article/pii/S0045782521002516. doi:https://doi.org/10.1016/j.cma.2021.113914.
[46] V. D. Nguyen, L. Noels, Micromechanics-based material networks revisited from the interaction viewpoint; robust and efficient implementation for multi-phase composites, European Journal of Mechanics - A/Solids 91 (2022) 104384. URL: https://www.sciencedirect.com/science/article/pii/S0997753821001431. doi:https://doi.org/10.1016/j.euromechsol.2021.104384.
[47] V. D. Nguyen, L. Noels, Interaction-based material network: A general framework for (porous) microstructured materials, Computer Methods in Applied Mechanics and Engineering 389 (2022) 114300. URL: https://www.sciencedirect.com/science/article/pii/S0045782521005934. doi:https://doi.org/10.1016/j.cma.2021.114300.
[48] W.-N. Wan, T.-J. Wei, T.-H. Su, C.-S. Chen, Decoding material networks: exploring performance of deep material network and interaction-based material networks, Journal of Mechanics 40 (2024) 796–807. URL: https://doi.org/10.1093/jom/ufae053. doi:10.1093/jom/ufae053. arXiv:https://academic.oup.com/jom/article-pdf/doi/10.1093/jom/ufae053/61156061/ufae053.pdf.
[49] T. Huang, Z. Liu, C. Wu, W. Chen, Microstructure-guided deep material network for rapid nonlinear material modeling and uncertainty quantification, Computer Methods in Applied Mechanics and Engineering 398 (2022) 115197. URL: https://www.sciencedirect.com/science/article/pii/S0045782522003498. doi:https://doi.org/10.1016/j.cma.2022.115197.
[50] N. Meyer, S. Gajek, J. Görthofer, A. Hrymak, L. Kärger, F. Henning, M. Schneider, T. Böhlke, A probabilistic virtual process chain to quantify process-induced uncertainties in sheet molding compounds, Composites Part B: Engineering 249 (2023) 110380. URL: https://www.sciencedirect.com/science/article/pii/S1359836822007533. doi:https://doi.org/10.1016/j.compositesb.2022.110380.
[51] T. Li, Micromechanics-informed parametric deep material network for physics behavior prediction of heterogeneous materials with a varying morphology, Computer Methods in Applied Mechanics and Engineering 419 (2024) 116687. URL: https://www.sciencedirect.com/science/article/pii/S0045782523008101. doi:https://doi.org/10.1016/j.cma.2023.116687.
[52] J. G. Jean, T.-H. Su, S.-J. Huang, C.-T. Wu, C.-S. Chen, Graph-enhanced deep material network: multiscale materials modeling with microstructural informatics, Computational Mechanics (2024). doi:https://doi.org/10.1007/s00466-024-02493-1.
[53] L. Wu, L. Adam, L. Noels, Micro-mechanics and data-driven based reduced order models for multi-scale analyses of woven composites, Composite Structures 270 (2021) 114058. URL: https://www.sciencedirect.com/science/article/pii/S0263822321005183. doi:https://doi.org/10.1016/j.compstruct.2021.114058.
[54] A. Li, J. J. Remmers, J. A. van Dommelen, T. J. Massart, M. G. Geers, A mean-field homogenization model for fiber reinforced composite materials in large deformation with plasticity, International Journal of Solids and Structures 310 (2025) 113200. URL: https://www.sciencedirect.com/science/article/pii/S0020768324005596. doi:https://doi.org/10.1016/j.ijsolstr.2024.113200.
[55] L. Wu, C. N. Chung, Z. Major, L. Adam, L. Noels, From sem images to elastic responses: A stochastic multiscale analysis of ud fiber reinforced composites, Composite Structures 189 (2018) 206–227. URL: https://www.sciencedirect.com/science/article/pii/S0263822317327770. doi:https://doi.org/10.1016/j.compstruct.2018.01.051.
[56] A. Cuitino, M. Ortiz, A material-independent method for extending stress update algorithms from small-strain plasticity to finite plasticity with multiplicative kinematics, Engineering computations 9 (1992) 437–437.
[57] V.-D. Nguyen, L. Wu, L. Noels, Unified treatment of microscopic boundary conditions and efficient algorithms for estimating tangent operators of the homogenized behavior in the computational homogenization method, Computational Mechanics 59 (2017) 483–505. URL: https://doi.org/10.1007/s00466-016-1358-z. doi:10.1007/s00466-016-1358-z.
[58] L. Wu, L. Noels, Data of "stochastic deep material networks as efficient surrogates for stochastic homogenisation of nonlinear heterogeneous materials", 2025. URL: https://gitlab.uliege.be/didearot/didearotPublic/publicationsData/2025_StochasticIBDMN. doi:10.5281/zenodo.15120313.